



iPTF15eqv: Multiwavelength Exposé of a Peculiar Calcium-rich Transient

Dan Milisavljevic¹, Daniel J. Patnaude¹, John C. Raymond¹, Maria R. Drout^{2,11}, Raffaella Margutti^{3,4}, Atish Kamble¹, Ryan Chornock⁵, James Guillochon¹, Nathan E. Sanders¹, Jerod T. Parrent¹, Lorenzo Lovisari¹, Igor V. Chilingarian^{1,6}, Peter Challis¹, Robert P. Kirshner¹, Matthew T. Penny⁷, Koichi Itagaki⁸, J. J. Eldridge⁹, and Takashi J. Moriya¹⁰

¹Harvard-Smithsonian Center for Astrophysics, 60 Garden St., Cambridge, MA 02138, USA

²The Observatories of the Carnegie Institution for Science, 813 Santa Barbara St., Pasadena, CA 91101, USA

³Center for Interdisciplinary Exploration and Research in Astrophysics (CIERA) and Department of Physics and Astrophysics, Northwestern University, Evanston, IL 60208, USA

⁴Center for Cosmology and Particle Physics, New York University, New York, NY 10003, USA

⁵Astrophysical Institute, Department of Physics and Astronomy, 251B Clippinger Lab, Ohio University, Athens, OH 45701, USA

⁶Sternberg Astronomical Institute, M.V.Lomonosov Moscow State University, 13 Universitetsky prospect, Moscow, 119992, Russia

⁷Department of Astronomy, Ohio State University, 140 West 18th Ave., Columbus, OH 43210, USA

⁸Itagaki Astronomical Observatory, Teppo-cho, Yamagata, Yamagata 990-2492, Japan

⁹Department of Physics, University of Auckland, Private Bag 92019, Auckland, New Zealand

¹⁰Division of Theoretical Astronomy, National Astronomical Observatory of Japan, National Institutes of Natural Sciences, 2-21-1 Osawa, Mitaka, Tokyo 181-8588, Japan

Received 2016 October 18; revised 2017 June 26; accepted 2017 June 29; published 2017 August 30

Abstract

The progenitor systems of the class of “Ca-rich transients” is a key open issue in time domain astrophysics. These intriguing objects exhibit unusually strong calcium line emissions months after explosion, fall within an intermediate luminosity range, are often found at large projected distances from their host galaxies, and may play a vital role in enriching galaxies and the intergalactic medium. Here we present multiwavelength observations of iPTF15eqv in NGC 3430, which exhibits a unique combination of properties that bridge those observed in Ca-rich transients and SNe Ib/c. iPTF15eqv has among the highest [Ca II]/[O I] emission line ratios observed to date, yet is more luminous and decays more slowly than other Ca-rich transients. Optical and near-infrared photometry and spectroscopy reveal signatures consistent with the supernova explosion of a $\lesssim 10 M_{\odot}$ star that was stripped of its H-rich envelope via binary interaction. Distinct chemical abundances and ejecta kinematics suggest that the core collapse occurred through electron-capture processes. Deep limits on possible radio emission made with the Jansky Very Large Array imply a clean environment ($n \lesssim 0.1 \text{ cm}^{-3}$) within a radius of $\sim 10^{17} \text{ cm}$. *Chandra X-ray Observatory* observations rule out alternative scenarios involving the tidal disruption of a white dwarf (WD) by a black hole, for masses $> 100 M_{\odot}$. Our results challenge the notion that spectroscopically classified Ca-rich transients only originate from WD progenitor systems, complicate the view that they are all associated with large ejection velocities, and indicate that their chemical abundances may vary widely between events.

Key words: galaxies: abundances – line: identification – stars: evolution – supernovae: general – supernovae: individual (iPTF15eqv, SN 2005E)

1. Introduction

An emergent class of transient objects defined by unusually strong calcium line emissions that develop in optical spectra months after explosion has garnered considerable attention in the last decade. These have been referred to as “Ca-rich,” (Filippenko et al. 2003), SN 2005E-like (Perets et al. 2010), and “Ca-rich gap” transients (Kasliwal et al. 2012). Here we adopt the broad classification of “Ca-rich transient.”

During the photospheric early stages, Ca-rich transients have distinct He lines in their spectra and fall within the supernova (SN) Type Ib classification (see Filippenko 1997, Gal-Yam 2016, and Parrent et al. 2016b for reviews of the SN classification scheme). However, Ca-rich transients are less luminous than normal SNe Ib and reach optically thin (i.e., “nebular”) stages within two months post-maximum light. During this stage, they exhibit a large emission line ratio [Ca II]/[O I] > 2 , which suggests that the total calcium synthesized is greater than that of normal SNe I, perhaps by factor of 5–10 (Perets et al. 2010). Estimates of their rates range from 2% to 12% of SNe Ia (Kasliwal et al. 2012).

The progenitors of Ca-rich transients are not confidently known. Stars with initial masses in the range of 8–12 M_{\odot} have been suggested (Kawabata et al. 2010; Suh et al. 2011), but unlike the majority of core-collapse SNe, many Ca-rich transients have been hosted by early-type galaxies lacking obvious massive star populations. Locations within dwarf galaxies or globular clusters is a possible resolution to this inconsistency (Yuan et al. 2013), but close examinations of explosion sites have thus far failed to uncover any sign of in situ star formation (Perets et al. 2011; Lyman et al. 2013, 2016; Lunnan et al. 2017). Gvaramadze et al. (2017) recently proposed that the Galactic supernova remnant RCW 86 formed from a core-collapse Ca-rich supernova that polluted the progenitor star’s solar-type binary companion that evolved through a common envelope phase.

Ca-rich transients are often found at large distances away from their host galaxies (as high as 150 kpc; Perets et al. 2010; Kasliwal et al. 2012; Perets 2014; Foley 2015). This intriguing property, combined with the lack of nearby stellar populations, has supported the notion that the progenitor systems have traveled significant distances before exploding (Lyman et al. 2014), perhaps via interaction with a supermassive black hole (BH; Foley 2015).

¹¹ Hubble, Carnegie-Dunlap Fellow.

The relatively large delay-time distribution required to travel large distances favors an older white dwarf (WD) population that also contributes to SNe Ia. Many explosion channels have been proposed, including helium detonations occurring on a helium-accreting WD (Shen & Bildsten 2009; Perets et al. 2010; Shen et al. 2010; Waldman et al. 2011; Woosley & Kasen 2011; Dessart & Hillier 2015; Meng & Han 2015), tidal disruptions of low-mass WDs by neutron stars or stellar-mass BHs (Metzger 2012; Fernández & Metzger 2013; Margalit & Metzger 2016), and tidal detonations of WDs caused by random flyby encounters with an intermediate mass BH (IMBH) in dwarf galaxies or globular clusters (Rosswog et al. 2008; MacLeod et al. 2014; Sell et al. 2015). Though the class has generally been treated uniformly, suspicions of heterogeneity in the progenitor system have been voiced (Kawabata et al. 2010; Lyman et al. 2014; Valenti et al. 2014; Sell et al. 2015; Lunnan et al. 2017).

Here we present and analyze the multiwavelength data set of a supernova exhibiting a revealing mix of properties that bridge Ca-rich transients and core-collapse SNe. Our observations are provided in Sections 2 and 3, our results in Section 4, and a detailed comparative analysis of the entire class of Ca-rich transients in Section 5. In Section 6, we review the ramifications of our conclusion that the progenitor system of the Ca-rich transient iPTF15eqv was most likely a massive star, and describe future observations and modeling required to understand the wide-ranging diversity encompassed in the Ca-rich transient observational classification.

2. iPTF15eqv

On 2015 September 27.81 (all dates UT), we reported the discovery of PSN J10520833+3256394 in NGC 3430 to the Central Bureau for Astronomical Telegrams “Transient Object Followup Reports” page.¹² Months later, an independent discovery was made by the intermediate Palomar Transient Factory (iPTF) on 2015 December 6 and designated iPTF15eqv (Cao et al. 2015), which we adopt here. Spectra obtained on 2015 December 07.53 by Cao et al. (2015) led them to classify iPTF15eqv as an SN IIB/Ib in the nebular phase.

Description of the spectrum noted weak continuum emission superposed by strong [Ca II] $\lambda\lambda 7291, 7324$ and weak H α emission lines. The lack of equally strong [O I] $\lambda\lambda 6300, 6364$ emission is unusual for an SN IIB/Ib and prompted our group to obtain optical spectra that confirmed the non-standard nature of the emissions.¹³ A multiwavelength follow-up campaign supported by radio observations with the Karl G. Jansky Very Large Array (VLA) and X-ray observations with the *Chandra X-ray Observatory* (CXO) was initiated.

Distance estimates to the host galaxy NGC 3430 range from 15.4 Mpc (Theureau et al. 2007) to 32.9 Mpc (Lagattuta et al. 2013). We adopt an estimate of 30.4 Mpc with distance modulus $\mu = 32.41 \pm 0.43$ (Sorce et al. 2014). NGC 3430 is classified as a Type SBc spiral by de Vaucouleurs et al. 1991, and also hosted the Type II SN 2004ez (Filippenko et al. 2004; Nakano et al. 2004).

Extinction toward iPTF15eqv appears to be minimal. Foreground extinction due to the Milky Way is

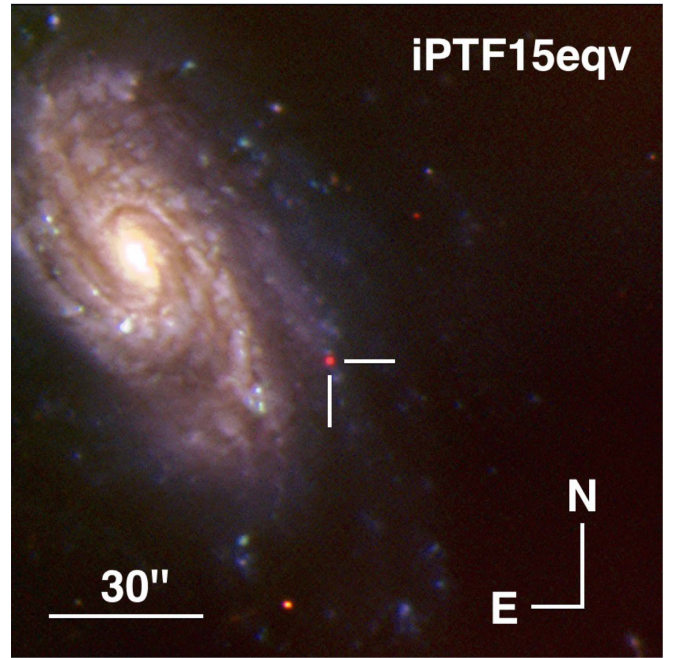


Figure 1. Composite image of iPTF15eqv and host galaxy NGC 3430 made from the MMT 6.5 m telescope + MMTCam observations obtained in the g' (blue), r' (green), and i' (red) bands. The red color of iPTF15eqv reflects the high equivalent width of the [Ca II] $\lambda\lambda 7291, 7324$ emission lines.

$E(B - V)_{\text{mw}} = 0.021$ mag (Schlafly & Finkbeiner 2011), there is no obvious suppression of flux at short wavelengths, and no conspicuous NaID absorption is observed in our optical spectra (see Section 3.2 for details). Thus, no correction for extinction has been adopted in this paper to the photometry or spectra. The one exception is an estimate of the metallicity of the host system (Section 4.4) that uses the relative strengths of the narrow emission lines associated with the environment around iPTF15eqv.

In Figure 1, we show a finding chart of iPTF15eqv made from images of the region obtained with the 6.5 m MMT telescope in combination with the MMTCam instrument¹⁴ in $g'r'i'$ -band filters. This composite image highlights the location of iPTF15eqv, which lies along an exterior spiral arm approximately $44''$ (≈ 6.5 kpc) from the host galaxy nucleus.

3. Observations

3.1. Optical Photometry

Unfiltered images of iPTF15eqv and its surrounding environment were obtained at Itagaki Observatory using the 0.60 m $f/5.7$, 0.50 m $f/6.0$, and 0.35 m $f/11.0$ telescopes mounted with a Bitran-CCD (Kodak KAF 1001E) detector¹⁵ between 2015 September 27 and December 18. We also obtained three epochs of MMTCam $r'i'$ -band photometry and one epoch of g' -band photometry between 2016 February 6 and June 8. A log of the observations is provided in Table 1, and a plot of the final photometry in Figure 2. Unless otherwise noted, uncertainties are quoted at the 1σ confidence level.

¹² <http://www.cbat.eps.harvard.edu/unconf/followups/J10520833+3256394.html>

¹³ Y. Cao also kindly provided the original classification spectrum for us to inspect.

¹⁴ <http://www.cfa.harvard.edu/mmti/wfs.html>

¹⁵ Specifications of the KAF 1001E detector can be found at http://www.onsemi.com/pub_link/Collateral/KAF-1001-D.PDF.

Table 1
Log of Optical Photometry

Date (UT)	Date (MJD)	Phase ^a (days)	Telescope + Instr.	Filter	Magnitude	σ
2015 Sep 27	57292.81	0	Itagaki Observatory	Clear	16.97	0.10
2015 Oct 06	57301.80	9	Itagaki Observatory	Clear	17.17	0.05
2015 Oct 16	57311.77	19	Itagaki Observatory	Clear	17.47	0.11
2015 Oct 20	57315.76	23	Itagaki Observatory	Clear	17.26	0.08
2015 Nov 04	57330.80	38	Itagaki Observatory	Clear	17.46	0.14
2015 Nov 12	57338.82	46	Itagaki Observatory	Clear	17.88	0.09
2015 Dec 12	57368.72	76	Itagaki Observatory	Clear	18.34	0.10
2015 Dec 18	57374.79	82	Itagaki Observatory	Clear	18.46	0.17
2016 Feb 06	57425.04	132	MMT+MMTCam	r'	19.70	0.06
2016 Feb 06	57425.05	132	MMT+MMTCam	i'	18.26	0.08
2016 Mar 11	57458.61	166	MMT+MMTCam	r'	20.35	0.10
2016 Mar 11	57458.62	166	MMT+MMTCam	i'	18.90	0.08
2016 Jun 08	57547.65	255	MMT+MMTCam	g'	22.12	0.09
2016 Jun 08	57547.65	255	MMT+MMTCam	r'	21.76	0.12
2016 Jun 08	57547.66	255	MMT+MMTCam	i'	20.90	0.09

Note. Unfiltered photometry should be interpreted as AB magnitudes.

^a Phase is with respect to the date of discovery on 2015 September 27.8 (MJD 57292.81).

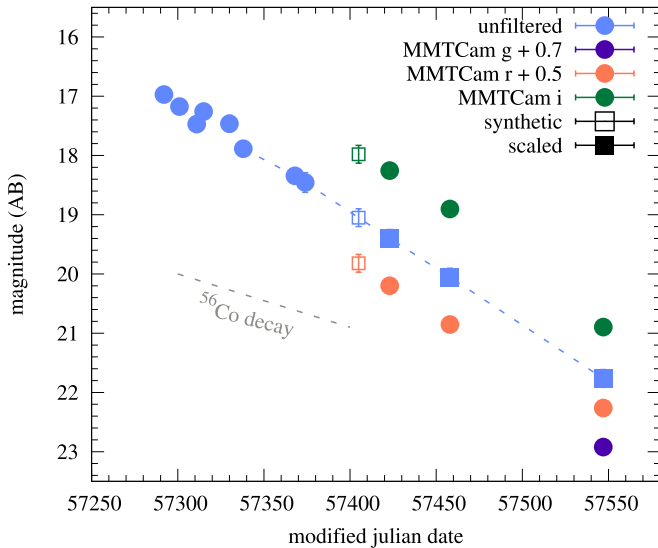


Figure 2. Photometry of iPTF15eqv. Unfiltered data are from Itagaki Observatory. Sloan $g'r'i'$ photometry is from MMT. Photometric measurements labeled “synthetic” are derived from optical spectroscopy, while those labeled “scaled” are derived from Sloan $g'r'$ photometry that has been corrected using color terms. Details are provided in the text.

Processing of the images was completed using standard routines in the Image Reduction and Analysis Facility (IRAF).¹⁶ This included bias, flat-field, and dark frame corrections, when available. Multiple images in a single night were stacked. We performed point-spread function photometry on iPTF15eqv and nearby field stars.

Absolute calibration was carried out using Sloan Digital Sky Survey (SDSS) observations of field stars. Approximate unfiltered magnitudes for the field stars were calculated by performing synthetic photometry on the SDSS $u'g'r'i'z'$ spectral energy distribution using the typical spectral response achieved

by the KAF 1001E detector in use at Itagaki Observatory. In addition, we subtract the flux associated with an ~ 21 mag stellar knot located $1''.5$ from iPTF15eqv from the unfiltered magnitudes measured from the Itagaki Observatory images. This stellar knot is well resolved and separated from the SN in our MMTCam observations, but would be included within the aperture used on the Itagaki Observatory images (typical resolution $\approx 4''$). This correction is $\lesssim 0.1$ mag for all epochs.

In order to directly compare the early unfiltered light curve to our late-time MMTCam observations, we performed synthetic photometry on a spectrum of iPTF15eqv obtained on 2016 January 18 (see Section 3.2) to investigate the relationship between the unfiltered magnitudes of the KAF 1001E detector and standard bandpasses. We verified the relationship using spectra of the Ca-rich transient SN 2005E (Perets et al. 2010). For transients with large $r' - i'$ colors (as is observed for iPTF15eqv at late times due to the large [Ca II] feature), we find an approximate relationship between the unfiltered and r' -band magnitudes, which ranges from $r' - \text{unf} = 0.0$ mag for $r' - i' = 0.85$ mag to $r' - \text{unf} = 0.3$ mag for $r' - i' = 1.45$ mag.

Applying these shifts to our MMTCam data, we obtain approximate unfiltered magnitudes for iPTF15eqv at late epochs that can be compared to the earlier phase data from Itagaki Observatory. These data are shown as open squares in Figure 2. We also plot unfiltered r' - and i' -band magnitudes obtained from our synthetic photometry. We do not attempt to transform the unfiltered magnitudes obtained from the Itagaki Observatory images to a standard bandpass since no spectral or color information is available at these epochs.

3.2. Optical Spectroscopy

Low-resolution optical spectra of iPTF15eqv were obtained using the MMT telescope in combination with the Blue Channel instrument (Schmidt et al. 1989) and the Hiltner 2.4 m telescope in combination with the Ohio State Multi-Object Spectrograph (OSMOS; Martini et al. 2011) instrument and R4K detector at MDM observatory. Conditions were photometric for most observations. Standard stars from Oke (1990) and Hamuy et al. (1992) were observed for spectrophotometric calibration and to remove telluric features. A log of all optical spectroscopy is provided in Table 2.

¹⁶ IRAF is distributed by the National Optical Astronomy Observatories, which are operated by the Association of Universities for Research in Astronomy, Inc., under cooperative agreement with the National Science Foundation.

Table 2
Log of Optical Spectroscopy

Date (UT)	Date (MJD)	Phase ^a (days)	Telescope + Instr.	Range (Å)	Resolution (FWHM in Å)
2015 Dec 31.5	57387.5	95	MDM 2.4m+OSMOS	5350–10500	6
2016 Jan 18.3	57405.3	112	MMT+Blue Channel	3360–8580	6
2016 Feb 15.3	57433.3	140	MMT+Blue Channel	3360–8580	6
2016 Mar 02.4	57450.4	158	MDM 2.4m+OSMOS	5350–10500	6
2016 Apr 14.2	57492.2	199	MMT+Blue Channel	3360–8580	6
2016 May 7–9	57517.3	225	MDM 2.4m+OSMOS	5350–10500	6

Note.

^a Phase is with respect to the date of discovery on 2015 September 27.8 (MJD 57292.8).

The Blue Channel observations used the B300 grating in combination with a 1'' slit width yielding spectra spanning a wavelength window of 3400–8500 Å and with resolution $R \sim 740$. OSMOS observations used a 1''2 slit width with the VPH-red grism and an OG530 order-blocking filter, resulting in spectra spanning a wavelength window of approximately 5500–10500 Å with resolution $R \sim 1200$.

Standard procedures to bias-correct, flat-field, and flux calibrate the data were followed using the IRAF/PYRAF software¹⁷ and our own IDL routines. Narrow and unresolved emission lines of [O II] $\lambda 3727$; [O III] $\lambda\lambda 4959, 5007$; H α ; H β ; and [S II] $\lambda\lambda 6716, 6731$ attributable to a coincident H II region were used to determine a recession velocity of 1494 km s^{-1} , which was removed from all spectra. A plot of the observations labeling prominent emission features is presented in Figure 3.

3.3. Near-infrared Spectroscopy and Photometry

A single epoch of low-resolution, near-infrared (NIR) spectra spanning 1–2.4 μm was obtained on 2016 March 23 with MMT using the MMT and Magellan Infrared Spectrograph (MMIRS) instrument (McLeod et al. 2012). Observations were made using a 0''6 slit width in three configurations: zJ filter (spanning 0.95–1.50 μm) + J grism ($R \sim 2000$), H filter (spanning 1.50–1.79 μm) + H3000 grism ($R \sim 3000$), and Kspec filter (spanning 1.95–2.45 μm) + K3000 grism ($R \sim 3000$). Exposure times were $4 \times 300 \text{ sec}$ for each configuration, and the slit was dithered between exposures. Data were processed using the standard pipeline (Chilingarian et al. 2015) to develop wavelength-calibrated 2D frames from which 1D extractions were made. A plot of these data combining all three individual spectra is shown in Figure 4. Line identifications are discussed in Section 4.2.

Acquisition images obtained in the J band were used to flux calibrate our NIR spectra. We performed aperture photometry on a stacked image made from pipeline-processed individual images, choosing an aperture to encompass all of the SN flux. 2MASS magnitudes of field stars provided a means of absolute calibration. We estimate the J-band magnitude of iPTF15eqv on 2016 March 23 to be $19.77 \pm 0.16 \text{ mag}$.

3.4. Chandra X-Ray Observations

We obtained deep X-ray observations of iPTF15eqv with CXO on 2016 January 4 under our approved program to explore stellar deaths at high energies and radio wavelengths (observation ID 16821, PI: Margutti). CXO data have been

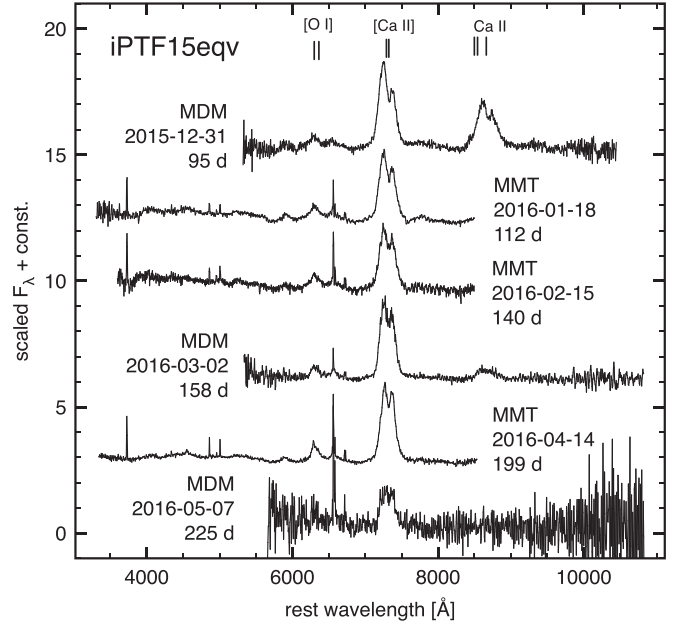


Figure 3. Six epochs of optical spectra of iPTF15eqv. Telescopes used, dates of observations, and phases with respect to the date of discovery on 2015 September 27.8 are provided. The three strongest emission lines, [Ca II] $\lambda\lambda 7291, 7324$; the Ca II triplet; and [O I] $\lambda\lambda 6300, 6364$, are identified.

reduced with the CIAO software v4.8 and corresponding calibration files. No X-ray source is detected at the location of iPTF15eqv with a total exposure time of 9.9 ks. The inferred 3σ count-rate limit is $4 \times 10^{-4} \text{ c s}^{-1}$ (0.5–8 keV). The neutral hydrogen column density in the direction of iPTF15eqv is $1.84 \times 10^{20} \text{ cm}^{-2}$ (Kalberla et al. 2005). For an assumed non-thermal spectrum with index $\Gamma = 2$, we derive an unabsorbed (absorbed) flux limit of $4.8 \times 10^{-15} \text{ erg s}^{-1} \text{ cm}^{-2}$ ($4.5 \times 10^{-15} \text{ erg s}^{-1} \text{ cm}^{-2}$) in the 0.3–10 keV energy range, corresponding to $5.3 \times 10^{38} \text{ erg s}^{-1}$ at the distance of iPTF15eqv.

3.5. Jansky Very Large Array Radio Observations

We obtained five epochs of radio observations of iPTF15eqv at frequencies ranging from 4.9 to 16.0 GHz with the VLA (PI: Margutti, program SG0534). All observations were taken in the standard continuum observing mode with a bandwidth of 16 IF \times 64 channel/IF \times 2 MHz/channel. The VLA changed configurations at various stages during these observations. During the reduction, we split the data into two side bands (8 IF

¹⁷ PYRAF is a product of the Space Telescope Science Institute, which is operated by AURA for NASA.

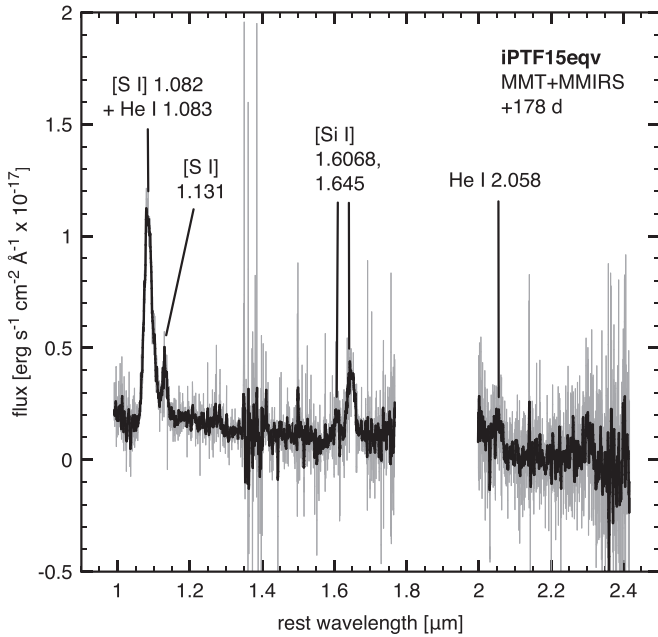


Figure 4. NIR spectrum of iPTF15eqv obtained on 2016 March 23 using the 6.5 m MMT telescope and MMIRS instrument. Line identifications are provided for the strongest emissions.

each) of approximately 1 GHz each. We used the radio source 3C 286 for flux calibration, and the calibrator J1018+3542 for phase referencing. Data were reduced using standard packages within the Astronomical Image Processing System. No radio emission was detected from iPTF15eqv in any of these observations resulting in deep flux density limits. The results are summarized in Table 3.

4. Results

4.1. Light Curve Evolution

We have utilized all photometric data of iPTF15eqv to compare it to the light curves of selected Ca-rich transients. Although our unfiltered photometry does not strictly match the *R*-band photometry, it does provide a reasonable means of comparing the slope and absolute luminosity of the light curve. As shown in Figure 5, iPTF15eqv was discovered at its peak observed unfiltered absolute magnitude of -15.4 , which is in the range of Ca-rich objects ($R \sim -15$ to -16.5 mag; Kasliwal et al. 2012; Valenti et al. 2014). The decline of the light curve of iPTF15eqv at a rate of ≈ 0.017 mag day $^{-1}$ is shallower than those of other Ca-rich transients at similar epochs. If we assume that iPTF15eqv was discovered around maximum light and shares the typical rise time of Ca-rich transients (12–15 days; Kasliwal et al. 2012), then the explosion date was approximately 2015 September 12. We refer to this as $t_{\text{exp}}(s1)$ and consider it a plausible scenario since the first reported spectrum of iPTF15eqv showing strong [Ca II] emissions by Cao et al. (2015) was obtained 70 days after discovery, which is within the time frame that Ca-rich transients exhibit pronounced Ca emissions.

However, because we do not have firm observational constraints on the explosion date, the light curve of iPTF15eqv may have peaked many weeks or months before the discovery date. To investigate this alternative scenario, we attempted to match the light curve of iPTF15eqv to that of SNe Ib/c

Table 3
Log of VLA Observations

Date (UT)	Date (MJD)	Frequency (GHz)	$3 \times \sigma_{\text{rms}}$ (μJy)	VLA Configuration
2015 Dec 24.57	57380.57	4.9	<318	D
2015 Dec 24.57	57380.57	7.1	<543	D
2016 Jan 05.60	57392.60	13.1	<45	DnC
2016 Jan 05.60	57392.60	16.0	<42	DnC
2016 Feb 18.48	57436.48	8.6	<42	C
2016 Feb 18.48	57436.48	11.0	<43	C
2016 May 22.22	57530.22	8.6	<33	B
2016 May 22.22	57530.22	11.0	<37	B
2016 Aug 03.08	57603.08	4.9	<67	B
2016 Aug 03.08	57603.08	7.1	<40	B
2016 Aug 03.08	57603.08	8.6	<38	B
2016 Aug 03.08	57603.08	11.0	<40	B

(Elmhamdi et al. 2006; Drout et al. 2011). By shifting the light curve of iPTF15eqv ≈ 50 days relative to the date of discovery, the overall slope and luminosity are comparable to the late-time linear decay rates found in other SNe Ib/c and consistent with expectations from ^{56}Co decay (Figure 5). A particularly good match was found with the light curve of SN 2011dh (Ergon et al. 2015). If this analogous connection to SN 2011dh is valid, then the first spectrum of iPTF15eqv was obtained some 120 days after the light curve peak that may have been as luminous as -17.5 mag. We refer to the explosion date of 2015 July 24 of this alternative scenario as $t_{\text{exp}}(s2)$. iPTF15eqv most likely exploded in the time interval $t_{\text{exp}}(s1) > t > t_{\text{exp}}(s2)$, and peaked in *R*-band absolute magnitude between approximately -17.5 and -15 .

If iPTF15eqv was, indeed, discovered after maximum light, then its light curve evolution can be approximately described by the nebular light curve model of Valenti et al. (2008), which is based on the instantaneous rate of energy deposition from the $^{56}\text{Ni} \rightarrow ^{56}\text{Co} \rightarrow ^{56}\text{Fe}$ decay chain (Arnett 1982). We investigated the range of viable explosion parameters for iPTF15eqv in this scenario. Model parameters include the total nickel mass, M_{Ni} , and a constant, F , which describes the incomplete trapping of gamma-rays. F is a function of the total ejecta mass M_{ej} , explosion kinetic energy E_{K} , and ejecta density distribution, and we adopt the parameterization of Valenti et al. (2008) such that $F \propto M_{\text{ej}}/\sqrt{E_{\text{K}}}$ (also see Clocchiatti et al. 1997). The luminosity of iPTF15eqv is estimated from the unfiltered light curve, assuming zero bolometric correction.

The range in mass of ^{56}Ni required to reproduce the luminosity of iPTF15eqv is degenerate with an adopted explosion date. The slope of the light curve rules out reasonable fits bracketing $t_{\text{exp}}(s1)$. However, for explosions bracketing $t_{\text{exp}}(s2)$ (i.e., 40–60 days prior to discovery), we obtain reasonable fits and constrain M_{Ni} to be between ≈ 0.04 – $0.07 M_{\odot}$ (Figure 6). In order to match the observed decay rate with this model, we require that $(M_{\text{ej}}/M_{\odot})(E_{\text{K}}/10^{51} \text{ erg})^{-0.5} = 3.0 \pm 0.1$. Assuming an average bulk explosion velocity at peak of $(7$ – $9) \times 10^3$ km s $^{-1}$ for Ca-rich transients (Kasliwal et al. 2012), we estimate $M_{\text{ej}} \approx 2$ – $4 M_{\odot}$ and $E_{\text{K}} \approx (0.8$ – $2) \times 10^{51}$ erg. These explosion parameters are comparable to those found for stripped-envelope SNe, including SN 2011dh (Bersten et al. 2012).

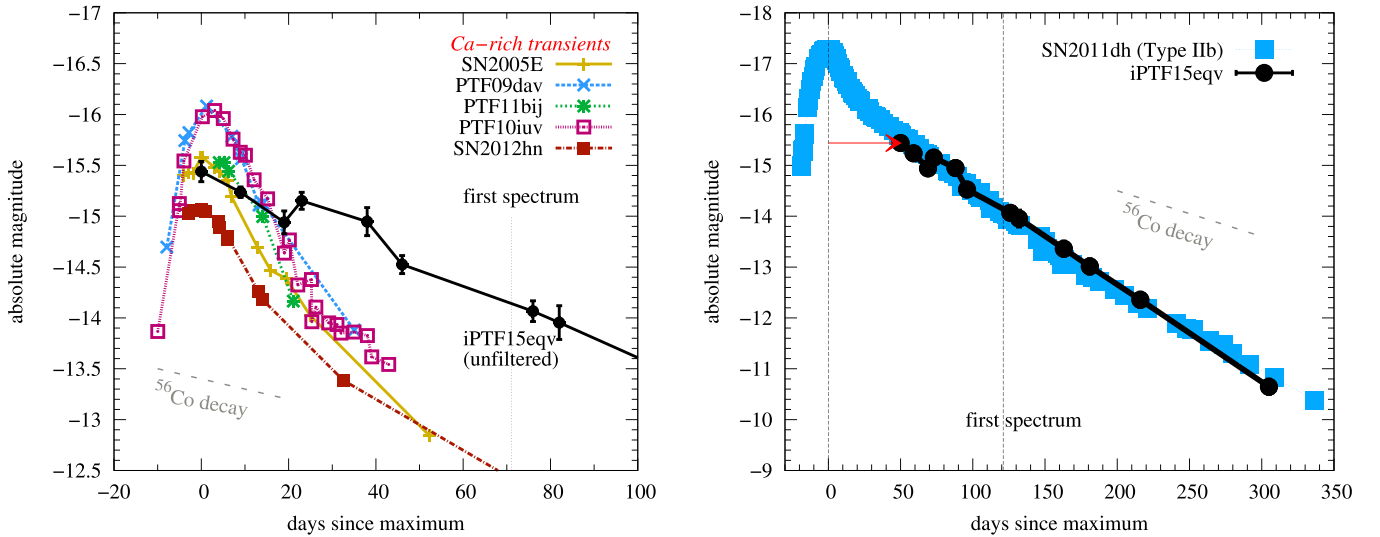


Figure 5. Comparing the unfiltered light curve of iPTF15eqv to that of Ca-rich transients and the Type IIb SN 2011dh. Left: absolute R -band light curves of Ca-rich transients. Here we assume that iPTF15eqv was discovered around maximum light. Because the Itagaki Observatory photometry is a non-standard combination of the R and I bands, the light curve of iPTF15eqv shown may deviate from its true R -band-only light curve by $\lesssim 0.3$ mag. Data are from Kasliwal et al. (2012) and Valenti et al. (2014). Right: R -band light curve of the Type IIb SN 2011dh. Data are from Ergon et al. (2015). Here we assume that the time of maximum light for iPTF15eqv was 50 days prior to the time of discovery. A distance modulus of $\mu = 32.41$ has been used, and no extinction has been corrected.

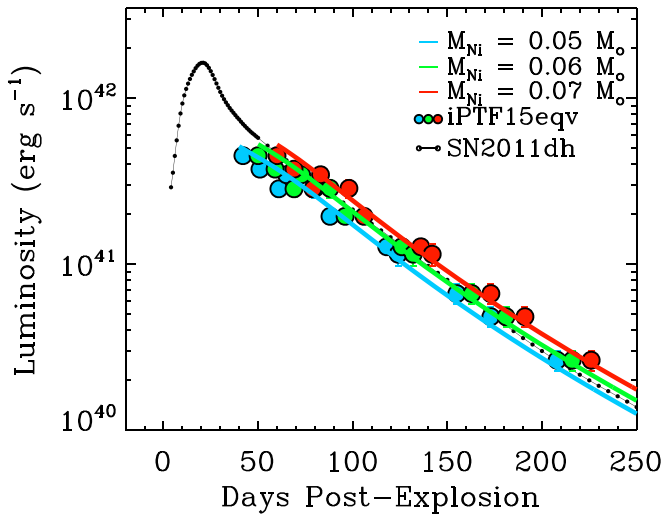


Figure 6. Estimating the explosion parameters M_{Ni} , E_k , and M_{ej} of iPTF15eqv assuming an explosion date around $t_{\text{exp}}(s2)$. Colored circles show the light curve of iPTF15eqv assuming the explosion occurred 40, 50, and 60 days prior to the discovery date of 2015 September 27 (cyan, green, and red, respectively). Colored lines show model fits to these light curves with 0.05, 0.06, and 0.07 M_{\odot} of ^{56}Ni , respectively. The bolometric light curve of SN 2011dh (Ergon et al. 2015) is shown for reference (black).

4.2. Emission Line Identification, Doppler Velocities, and Evolution

The dominant emission feature of iPTF15eqv over all observed epochs is [Ca II] $\lambda\lambda 7291, 7324$ (Figure 3). The Ca II NIR triplet $\lambda\lambda 8498, 8542$, and 8662 is strong on day 95, but has faded by day 158. The critical density for the [Ca II] doublet is $\sim 3 \times 10^6 \text{ cm}^{-3}$ from CHIANTI v7 (Landi et al. 2013), so this threshold may have been reached during the observed epochs, but the ratio also depends on temperature.

Also unambiguously detected is [O I] $\lambda\lambda 6300, 6364$. The ratio of [Ca II]/[O I] ≈ 10 exhibits little change over the entire observing period. We attribute emission centered around 5890 Å to a blend of Na I and He I 5876. The central

wavelength of the observed distribution favors Na I as the dominant ion, but helium is inferred to be a potential contributor because Ca-rich transients show helium in early spectra, and there is evidence of He I lines in the NIR.

We identify a feature centered near 6560 Å as $H\alpha$ or Ca I] $\lambda 6572$. The central wavelength of the feature favors $H\alpha$. However, the lack of $H\beta$ emission, the extremely strong [Ca II] lines, the large Ca I] $\lambda 6572$ collision strength (Samson & Berrington 2001), and the presence of [Si I] and [S I] in the NIR spectrum all suggest that Ca I] $\lambda 6572$ may be strong. [N II] $\lambda\lambda 6548, 6583$ may also contribute to the profile (Jerkstrand et al. 2015).

In the day 199 spectrum, a minor emission peak is observed around 4550 Å. We attribute this to blueshifted Mg I] $\lambda 4571$. An alternative identification of Si I $\lambda 4589$ seems unlikely since its stronger companion line $\lambda 7725$ is not detected. Also seen in the day 199 spectrum is a “plateau” of emission between 4000 and 5600 Å. This emission is not uncommon in SNe Ib/c (see, e.g., Milisavljevic et al. 2013b), and is due largely to iron-peak elements.

We show the emission line profile distributions for a variety of ions in Figure 7. The [Ca II] lines exhibit the largest velocities. With respect to the $\lambda 7291$ line measured toward short wavelengths and the $\lambda 7324$ line measured toward long wavelengths, the emission is above the continuum level for velocities up to and potentially exceeding $\sim 10^4 \text{ km s}^{-1}$. The profile has a central absorption notch centered around $+750 \text{ km s}^{-1}$ situated between two peaks at velocities of -1700 and $+2600 \text{ km s}^{-1}$. The blue/red ratio between peaks decreases from 3:1 to 3:2 over the epochs observed. The central dip in [Ca II] $\lambda\lambda 7291, 7324$ does not correspond to the separation of the lines (1400 km s^{-1}) and must be due to geometry or optical depth. On the other hand, the Ca triplet on day 95 shows a similar dip, but it is redshifted by $\approx 4000 \text{ km s}^{-1}$ and the peaks correspond to the separation between the two strongest lines of the triplet. The triplet is almost certainly optically thick, and radiative transfer must play an important role.

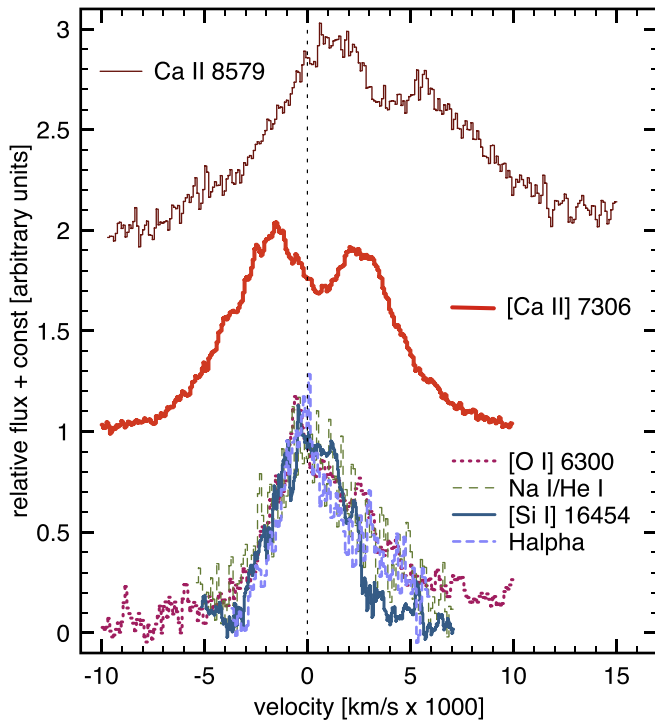


Figure 7. Emission line profiles of iPTF15eqv enlarged around the Ca II near-infrared triplet; [Ca II] $\lambda\lambda$ 7291, 7324; [O I] $\lambda\lambda$ 6300, 6364; [Si I] λ 16454; and H α . Velocities are with respect to 8579, 7306, 6300, 16454, and 6563 Å, respectively. From the H α profile, we have removed strong and unresolved H α and [N II] lines from a coincident H II region, and a linearly sloped continuum introduced from blending with the nearby [O I] profile. See Section 4.2 for a discussion of why the H α emission feature may have significant contribution from Ca I] λ 6572.

The [O I], Na I/He I blend, and H α /Ca I]/[N II] blend all have velocity spans much less than that of [Ca II] and do not share the double-peaked distribution. The measurement is complicated by a nonlinear continuum and blending of features, but generally for all emission lines except for calcium we measure maximum velocities in the region of $\approx 3400 \text{ km s}^{-1}$. Nonuniform density, uneven ^{56}Co heating, and chemical stratification are all possible reasons for the observed line asymmetry. An important consideration is that Ca is relatively easy to ionize (Ionization Potential = 6.11 eV) compared to Si (IP = 8.51 eV) and S (IP = 10.34 eV), and that the neutral gas may be expanding more slowly. In principle, if the radioactive material were evenly mixed, the heating would be proportional to n and the cooling (if optically thin) proportional to n^2 , so denser regions would be cooler and more neutral.

The emission feature centered near $1.64 \mu\text{m}$ could potentially be ascribed to [Fe II], but the absence of the stronger [Fe II] line at $1.257 \mu\text{m}$ makes this impossible. Instead, the $1.64 \mu\text{m}$ line must be [Si I] $1.645 \mu\text{m}$, an identification confirmed by the $1.6068 \mu\text{m}$ [Si I] line with the intrinsic 1:3 intensity ratio for this pair of lines.

The presence of the [Si I] line pair suggests that the lines at 1.08 and $1.13 \mu\text{m}$ could be the corresponding [S I] 1.0824 and $1.1309 \mu\text{m}$ lines, rather than the He I 1.083 and O I $1.129 \mu\text{m}$ lines near these wavelengths (e.g., Jerkstrand et al. 2015). The absence of the O I $1.317 \mu\text{m}$ line and the O I multiplet at 7774 Å , which should be 30 times stronger than the $1.129 \mu\text{m}$ line, rules out the O I identification and places an upper limit of 10% to the O I contribution to the $1.13 \mu\text{m}$ feature.

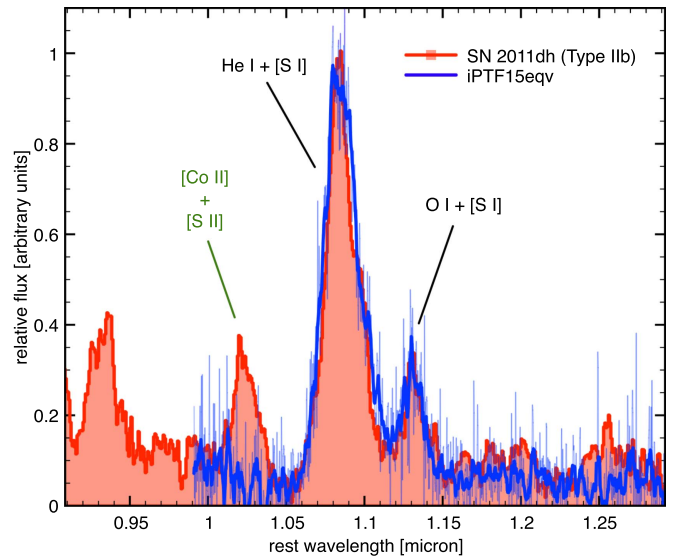


Figure 8. NIR spectra of iPTF15eqv (this paper) and SN 2011dh (Ergon et al. 2015) in the region of $0.95\text{--}1.25 \mu\text{m}$. Emission peaks at 1.083 and $1.125 \mu\text{m}$ are common to both, but only SN 2011dh has an emission peak at $1.03 \mu\text{m}$.

The measured intensity ratio $I(1.08)/I(1.13)$ is 4.2:1, rather than the 3.4:1 ratio given by the [S I] Einstein A values, suggesting that He I may indeed contribute to the $1.08 \mu\text{m}$ line. [Si I] $1.099 \mu\text{m}$ may also contribute to the feature (Fransson & Chevalier 1989; Jerkstrand et al. 2015). A feature consistent with He I $2.058 \mu\text{m}$, which should be a few times fainter than the $1.083 \mu\text{m}$ line, is marginally detected (Figure 4). The optical spectra indicate an upper limit to the He I 5876 line of $1.3 \times 10^{-15} \text{ erg cm}^{-2} \text{ s}^{-1}$, which would indicate an upper limit of 12% contribution of He I to the $1.08 \mu\text{m}$ feature. This is within the measurement uncertainties of the value of 20% indicated by the difference between the observed line ratio and the intrinsic [S I] intensity ratio. We note that the [Si I] and [S I] lines have very low excitation thresholds, so that they can be excited in fairly cool gas, while the He I and O I lines are produced by recombination and require ionized helium and oxygen. The absence of [S II] $1.03 \mu\text{m}$ emission while [S I] emission is strong (Figure 8) implies either predominantly neutral sulfur or very cool gas.

4.3. Chemical Abundances

We estimated chemical abundances of the ejecta of iPTF15eqv using the relative line strengths and luminosities of the ions identified in our optical and NIR spectra. The ratio of the Ca triplet to the [Ca II] lines at 7300 Å depends on temperature and density. On day 95, the ratio is 0.7, while on day 158 it has fallen to 0.1. The Ca triplet lines are produced by the decay of the $4p$ level, which decays by way of the H and K lines at $3933, 3968 \text{ Å}$ 94% of the time. However, for large optical depths in H and K, nearly all the H and K photons will be converted to triplet photons, which escape because of the smaller optical depth.

Using atomic rates from CHIANTI version 8 (Del Zanna et al. 2015) and assuming that all excitations to the $4p$ level produce Ca triplet photons, we compute the [Ca II]/Ca II ratio as a function of electron density (n_e) and temperature (T). We restrict the temperature range to $3.9 < \log T < 4.1$. At lower temperatures, a Ca I:Ca II ratio above 0.1 would imply that the Ca I] line at $\lambda 6572$ would exceed the intensity of the observed

6560 Å feature (based on the Ca I] excitation rate from Samson & Berrington 2001). At higher temperatures, Ca would be ionized to Ca III and ions such as O II and S II are expected to be strong. None of these higher ionization states are observed (see Figures 3 and 4). The allowed density range within these constraints is $10^{5.9} \text{ cm}^{-3}$ at $\log T = 4.1$ to $10^{6.7} \text{ cm}^{-3}$ at $\log T = 3.8$.

Between day 95 and day 158, the 7300 Å flux drops by a factor of 4.6, while the Ca triplet flux drops by a factor of 20. Homologous expansion during that interval implies that the density drops by a factor of 4.6. The flux changes in both lines can be matched with a factor of 4.6 drop in density and a factor of about 1.4 drop in temperature. That is a smaller change than the factor of 2.8 from adiabatic expansion alone, indicating that radioactive heating partly compensates for adiabatic cooling.

The [O I] and [Ca II] lines have similar excitation potentials and critical densities, thus their intensity ratio depends relatively weakly on temperature and density. In the temperature range derived above, most of the oxygen is neutral and most of the calcium is Ca II, so that the intensity ratio of the lines reflects the Ca to O abundance ratio. Since the [O I] to [Ca II] ratio is nearly constant at ≈ 0.1 during our observations, but the emissivity of [Ca II] is much larger than that of [O I] according to CHIANTI version 8 (Del Zanna et al. 2015), the O:Ca abundance ratio (by number) is 39 ± 24 . The substantial range is due to the range of temperature and density derived above.

The relative excitation rates of [S I] and [Ca II] vary less with density and temperature than those of [O I] and [Ca II], but the uncertainty in the flux calibration of the NIR spectrum and the necessity to interpolate the [Ca II] fluxes between nearby observations dominate the measurement uncertainty. We also assume that one-fifth of the $1.089 \mu\text{m}$ emission comes from He I to match the $1.089\text{--}1.131 \mu\text{m}$ intensity ratio. We use CHIANTI version 8 to predict the S I emissivities. Notably, Table 3 of Tayal (2004) mislabels the collision strengths from levels 1 and 3 to levels 4 and 5, and we have corrected the corresponding data file. We find a S:Ca abundance ratio of 29 ± 7 .

The [Si I] lines suffer from a still higher calibration uncertainty and greater difficulties in removing night sky lines. Using the excitation cross-section of Pindzola et al. (1977) and an Einstein A value of 0.0037, we find that the [Si I] emissivity is 5–10 times smaller than the [S I] emissivity over the range of density and temperature that we infer. The [Si I] flux is one-third that of the [S I] lines, suggesting the Si abundance is 1.7 to 3.3 times as large as that of S. However, since the [Si I] excitation rate did not include resonances or cascades, it may be an underestimate.

At a distance of 30.4 Mpc, the [Ca II] luminosity is $3.5 \times 10^{40} \text{ erg s}^{-1}$. With emissivities of $(2.0 \pm 0.6) \times 10^{-13} \text{ erg s}^{-1}$ per atom, that implies a calcium mass of $0.006 \pm 0.002 M_{\odot}$. The masses of oxygen, silicon, and sulfur are about $0.09^{+0.11}_{-0.08}$, 0.31 ± 0.2 , and $0.14 \pm 0.08 M_{\odot}$, respectively.

If we assume that the nebular emission arises in a shell given by a velocity of 3400 km s^{-1} , or $R = 2.8 \times 10^{15} \text{ cm}$ at day 95, and that the thickness of the shell is $R/8$ because of a steep ($n \propto R^{-9}$) density distribution, the density of Ca II ions is $5 \times 10^6 \text{ cm}^{-3}$. As this lies within the electron density range derived above, it is at least plausible that calcium provides most of the free electrons in the nebular shell.

There are many caveats to our estimates. Absorption may obscure interior emission (Taubenberger et al. 2009; Milisavljevic et al. 2010), the ejecta may be clumpy (Spyromilio 1994; Milisavljevic et al. 2012), and our assumption that all lines are formed in the same volume may be incorrect. Indeed, indications that some degree of asymmetry in the ejecta not accounted for in our estimates can be seen in the clear asymmetry in the line profiles (Figure 7). Furthermore, there is noticeable discrepancy between the masses we obtain from fitting the light curve (Section 4.1) and from the spectra. Our spectral analysis may not be accounting for all masses because much of the mass is at undetectable low densities and/or temperatures. This is especially true for H and/or He material that may be neutral and at temperatures that are too low for any significant excitation. Improved chemical abundances and mass estimates may be possible with a more sophisticated model that includes radiative transfer and additional assumptions about ejecta kinematics.

4.4. Metallicity and Star Formation Rate

Unlike many Ca-rich transients that are discovered in isolated locations, iPTF15eqv is within the projected proximity of a fairly rich environment of hot gas and stars (Figure 1). Using our optical spectra, we estimated the metallicity of the region surrounding the explosion site of iPTF15eqv using the Markov Chain Monte Carlo method of Sanders et al. (2012b) to model the emission line spectra and measure the fluxes of the strong emission lines. Following this approach, we estimate the oxygen abundance as $\log(\text{O}/\text{H}) + 12 = 8.65 \pm 0.04$ and 8.58 ± 0.02 using the N2 and O3N2 diagnostics, respectively, of Pettini & Pagel (2004), and as $\log(\text{O}/\text{H}) + 12 = 8.82 \pm 0.07$ using the diagnostic of Kewley & Dopita (2002) (KD02). These metallicity estimates are consistent given the characteristic offsets between the diagnostics (Kewley & Ellison 2008) and uncertainties, and correspond to a metallicity of $\sim 0.8 Z_{\odot}$. The quoted uncertainty is not inclusive of systematic effects such as the calibration variance in the strong line metallicity diagnostics (~ 0.1 dex, Kewley & Ellison 2008) or local metallicity variation in the host galaxy (as much as 0.3 dex; Sanders et al. 2012a, 2012b).

NGC 3430 is in the imaging footprint of the SDSS, which allowed us to make use of the SDSS-calibrated luminosity–metallicity–color relation (LZC) of Sanders et al. (2013) to infer an independent estimate of galaxy metallicity from optical luminosity and color. Using the extinction-corrected absolute magnitudes of the host galaxy in the SDSS DR12 cModel magnitudes (Schlafly & Finkbeiner 2011; Alam et al. 2015), $M_g = -19.439 \text{ mag}$, and $M_r = -20.042 \text{ mag}$, the LZC photometric metallicity for NGC 3430 is $\log(\text{O}/\text{H}) + 12 = 8.68$ with a characteristic scatter of 0.07 dex in the Pettini & Pagel (2004) N2 diagnostic calibration of the LZC relation.

We also estimated the star formation rate (SFR) density of the explosion site using the [O II] and H α line fluxes measured from our optical spectra. We measure an [O II] $\lambda 3727$ brightness of $9.7 \times 10^{40} \text{ erg s}^{-1} \text{ arcsec}^2$ and an H α luminosity of $1.3 \times 10^{41} \text{ erg s}^{-1} \text{ arcsec}^2$, with an estimated uncertainty in our spectrophotometric flux calibration of 20%. Using the [O II] SFR diagnostic of Kewley et al. (2004), assuming a distance scale of $0.102 \text{ kpc arcsec}^{-1}$, and assuming the KD02 metallicity quoted above, we find an explosion site SFR density of $(60 \pm 10) \times 10^{-3} M_{\odot} \text{ yr}^{-1} \text{ kpc}^{-2}$. Using the H α diagnostic of Moustakas et al. (2006), we find an SFR density of $(80 \pm 20) \times 10^{-3} M_{\odot} \text{ yr}^{-1} \text{ kpc}^{-2}$. Given the uncertainty in the flux calibration, the two estimates are similar. Both

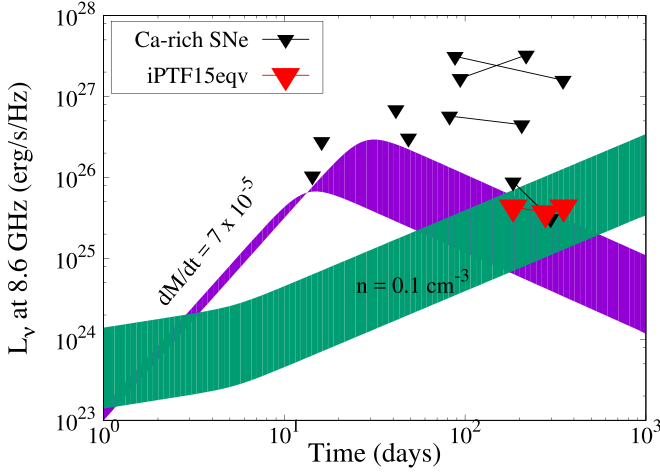


Figure 9. Upper limits of radio emission at 8.6 GHz from iPTF15eqv (red) compared to those of other Ca-rich transients published in Chomiuk et al. (2016; black). The purple shaded region represents the radio luminosity due to the wind-like medium with $\dot{M} = 7 \times 10^{-5}$ for the progenitor wind velocity of 100 km s^{-1} . The green shaded region represents an ISM-like medium with a density of 0.1 cm^{-3} . The width of the shaded regions represents the spread due to $0.01 \leq \epsilon_B \leq 0.1$ and $\epsilon_e = 0.1$. We used $E_K = 10^{51} \text{ erg}$ and $M_{ej} = 2 M_\odot$ (Section 4.1).

approaches indicate a vigorous SFR consistent with the morphological type of the galaxy.

4.5. Radio Synchrotron Limits

The radio emission in SNe is due to synchrotron radiation. As the forward shock wave moves through the surrounding circumstellar and interstellar material (CSM and ISM), a fraction of its kinetic energy gets converted into motion of the shock-accelerated particles. The relativistic electrons behind the shock are the main radiators that gyrate in the shock-amplified magnetic field and radiate synchrotron radiation (Chevalier 1982). The energy distribution of these relativistic electrons is a power law, $n_e(\gamma_e) \propto \gamma_e^{-p}$, with index p and the Lorentz factor γ_e of individual electrons. This form of the electron distribution is often evident from the synchrotron radio spectrum of SNe. Thus, we can utilize our deep radio observations of iPTF15eqv to probe unique information about its immediate environment.

For a constant mass-loss rate and wind velocity, the density in the stellar environment falls with the distance as the inverse squared, $\rho \propto r^{-2}$. In a typical massive star, this wind-density profile may extend to several parsecs. A typical supernova shock wave traveling at the speed of a few $\times 10^4 \text{ km s}^{-1}$ may take several decades before crossing the progenitor wind.

We followed procedures outlined in Kamble et al. (2014), based on work by Chevalier (1982, 1998), and Chevalier & Fransson (2006) to estimate the radio emission generated by a shock wave expanding in such an environment. The deep upper limits on radio brightness evolution at 8.6 GHz constrain the progenitor wind mass-loss rate to be $\dot{M} \lesssim 7 \times 10^{-5} M_\odot \text{ yr}^{-1}$ assuming a constant wind velocity of $v_w = 100 \text{ km s}^{-1}$. This is shown in Figure 9 by the purple shaded region. We also show the expected radio light curves for the ISM density profile. Our observations constrain the ISM density to be $n \lesssim 0.1 \text{ cm}^{-3}$. The width of the shaded regions represents the spread due to the $0.01 \leq \epsilon_B \leq 0.1$ and $\epsilon_e = 0.1$, where ϵ_B and ϵ_e are the

fractions of the kinetic energy channeled into the post-shock magnetic fields and shock-accelerated relativistic electrons, respectively.

4.6. Tidal Disruption

One model of Ca-rich transients is that they are tidal disruptions of low-mass WDs by IMBHs (Rosswog et al. 2008; Metzger 2012; MacLeod et al. 2014; Sell et al. 2015; Tanikawa et al. 2017). MacLeod et al. (2016) provide observable signatures of this process at optical wavelengths. We find that our overall light curve evolution is not consistent with extrapolations of their models that generally show much flatter and nearly constant evolution in the R and I bands, and we do not have photospheric epoch spectra to compare with their synthetic spectra.

However, a unique signature of tidal detonations by IMBHs is that they are accompanied by the fallback of substantial amounts of stellar debris returning to the BH that can be accreted and emit at X-ray wavelengths. Our *CXO* observations of iPTF15eqv can be used to constrain the likelihood of this scenario.

The fallback rate can be several orders of magnitude above the Eddington limit (MacLeod et al. 2016), with the inner X-ray emitting portions of the accretion structure being potentially obscured by optically thick material. While a jet can be produced during this hyper-accretive phase, the absence of any detected afterglow suggests that no jet was formed. The disk produced by the fallback will be able to radiate at roughly its Eddington limit during this phase,

$$L_{\text{Edd}} \equiv GM_{\text{h}} m_p c / \sigma_T \simeq 10^{41} M_{\text{h},3} \text{ erg s}^{-1},$$

where $M_{\text{h},3}$ is the BH mass in units of $10^3 M_\odot$. Using the peak accretion rate and time found in simulations (Guillochon & Ramirez-Ruiz 2013), the timescale wherein the fallback rate will remain above the Eddington limit is

$$t_{\text{Edd}} = 1 M_{\text{h},3}^{-2/5} M_{\text{WD},0.6}^{1/5} R_{\text{WD},0.6}^{3/5} \text{ year},$$

where $M_{\text{WD},0.6}$ and $R_{\text{WD},0.6}$ are the mass and radius of an $0.6 M_\odot$ WD. MacLeod et al. make the point that viscous effects may act to spread the accretion of matter over somewhat longer timescales, prolonging the time that the accretion rate remains above Eddington up to a factor of ~ 10 . After this phase, the accretion luminosity should decay approximately as $(t/t_{\text{peak}})^{-5/3}$ (Rees 1988).

Sell et al. (2015) observed SN 2012hn 533 days after the explosion to look for accretion emission during the decay phase. No emission was detected, and from an X-ray upper limit on the luminosity of $L_{0.5-8\text{keV}} < 4.4 \times 10^{38} \text{ erg s}^{-1}$ they concluded that SN 2012hn was unlikely to be a tidal detonation by an IMBH unless the BH is at the low end of the IMBH mass distribution. Our upper-bound limit on the luminosity ($< 5.3 \times 10^{38} \text{ erg s}^{-1}$) of iPTF15eqv is comparable to that of SN 2012hn, but since our observation of iPTF15eqv was closer to the time of explosion than SN 2012hn (114–164 days versus 533 days), we can place even stricter constraints on the IMBH mass. Given that we would expect the accretion disk to be radiating at close to its Eddington limit for nearly a year and decline rapidly afterwards, and that even the 10% accretion efficiency expected in the low-hard state (as assumed in Sell et al. 2015) would have been detected, we can restrict the BH

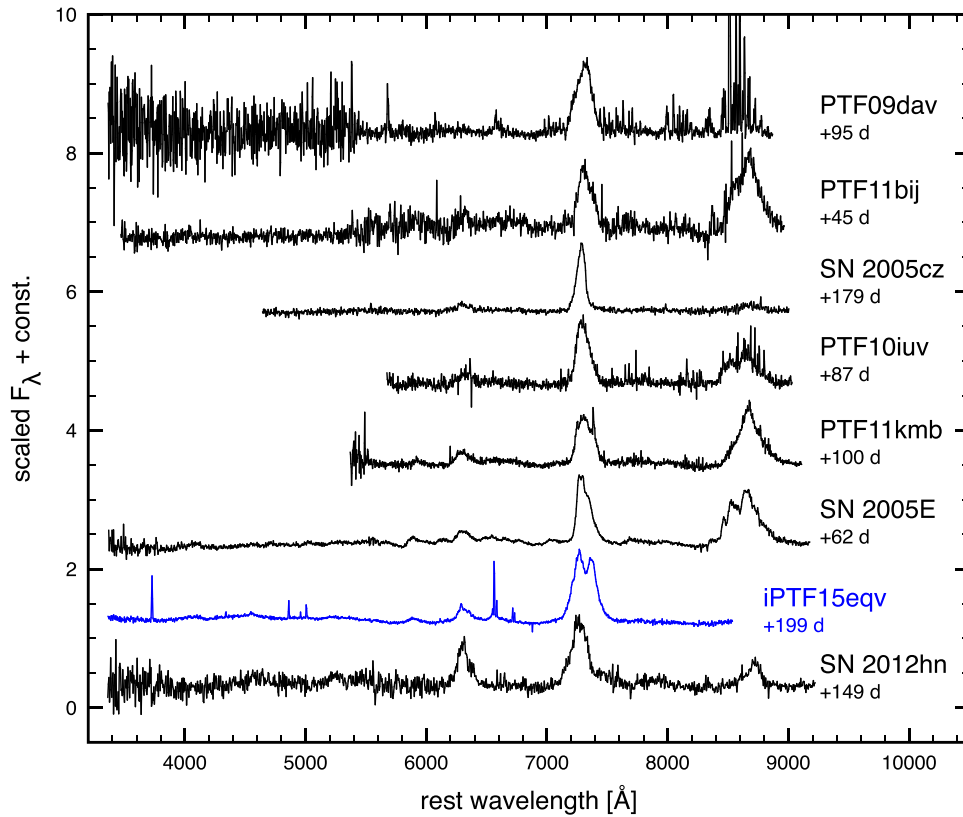


Figure 10. Optical spectra of Ca-rich transients compared to that of iPTF15eqv. Archival data were originally published in Kawabata et al. (2010), Perets et al. (2010), and Kasliwal et al. (2012) and have been obtained through WISEREP (Yaron & Gal-Yam 2012) and the OSC (Guillochon et al. 2017).

mass to the point that only a stellar mass BH ($\lesssim 100 M_{\odot}$) could yield $t_{\text{Edd}} < 164$ days.

Our constraint on the BH mass falls into the regime of a “micro” tidal disruption event (Metzger 2012; Perets et al. 2016), a scenario that would only be likely in a dense stellar cluster where close encounters between stars are common. In these models, a sufficiently massive WD is tidally disrupted by its BH companion as the binary orbit shrinks due to unstable mass transfer. The WD debris is sheared into an accretion disk with an initial size that is comparable to that of the initial binary at the time of Roche-lobe overflow.

5. Discussion

iPTF15eqv exhibits a unique combination of properties that bridge those observed in Ca-rich transients and SNe Ib/c. On the one hand, the late-time spectra of iPTF15eqv are dominated by strong calcium emission lines, which is a defining characteristic of Ca-rich transients. We illustrate this similarity in Figure 10, where we show the day 199 spectrum of iPTF15eqv and a sample of Ca-rich transients from the literature. On the other hand, iPTF15eqv differs from other Ca-rich transients in terms of its light curve evolution. iPTF15eqv was a slower evolving and potentially much more luminous object than Ca-rich transients and exhibited a light curve that resembles SNe Ib/c (Figure 5). Below we explore how to place iPTF15eqv within the Ca-rich transient classification and seek to understand whether a single progenitor system framework can unite their diverse properties.

5.1. $[\text{Ca II}]/[\text{O I}]$

For Ca-rich transients having optical spectra publicly accessible through the Weizmann Interactive Supernova Data Repository (WISEREP; Yaron & Gal-Yam 2012) and the Open Supernova Catalog (OSC; Guillochon et al. 2017), we measured the $[\text{Ca II}]/[\text{O I}]$ relative flux ratio (for cases where both lines could be observed) to determine the range of ratios encountered thus far in the literature. Multiple epochs were measured when possible. The results are listed in Table 4 and plotted in Figure 11. For comparison, we also measured this ratio for a number of H-rich (Type II) and H-poor (Type Ib/Ic) SNe. At all epochs where both lines are visible and the conditions can be reasonably assessed to be nebular, all Ca-rich transients have $[\text{Ca II}]/[\text{O I}] > 2$ and all Type Ib/c are < 2 . iPTF15eqv exhibits the strongest $[\text{Ca II}]/[\text{O I}]$ emission ratio (≈ 10) in our sample. SNe II typically have higher $[\text{Ca II}]/[\text{O I}]$ ratios between ≈ 2 –4. However, the phase at which this ratio is observed in SNe II ($t > 200$ days) is much later than Ca-rich transients ($50 < t < 150$ days).

Notably, the ratio of $[\text{Ca II}]/[\text{O I}]$ for many SNe Ib/c can decrease with time. For example, a 30% change in the ratio was noted in SN 2004gq between day 258 and 381 (Kuncarayakti et al. 2015). For this reason, Valenti et al. (2014) raised the issue that the high $[\text{Ca II}]/[\text{O I}]$ ratio seen in some Ca-rich transients at relatively early phases may in part be a phase-dependent effect rather than reflecting an intrinsic abundance pattern.

In the case of iPTF15eqv, the $[\text{Ca II}]/[\text{O I}]$ ratio exhibited modest change between the epochs where both features were well observed (i.e., days 95–199; Figure 3). This lack of

Table 4
[Ca II]/[O I] Ratio of SN Ib/c and Ca-rich Transients

Object	[Ca II]/[O I]	Phase (Days Post-maximum)	Type	References
iPTF15eqv	11.3	95 ^a	Ca-rich	This paper
iPTF15eqv	9.5	199 ^a	Ca-rich	This paper
SN2005cz	7.5	179	Ca-rich	Kawabata et al. (2010)
PTF10iuv	6.8	87	Ca-rich	Kasliwal et al. (2012)
PTF11kmb	4.6	100	Ca-rich	Foley (2015)
SN 2005E	7.3	62	Ca-rich	Perets et al. (2010)
SN 2012hn	2.5	149	Ca-rich	Valenti et al. (2014)
PTF11bij	4.4	45 ^a	Ca-rich	Kasliwal et al. (2012)
SN 2003dr	9.6	76 ^a	Ca-rich	Kasliwal et al. (2012)
SN 1999em	4.2	313	IIP	Leonard et al. (2002)
SN 2004dj	1.8	252	IIP	OSC
SN 2004et	3.0	301	IIP	Sahu et al. (2006)
SN 2004et	3.3	391	IIP	Sahu et al. (2006)
SN 2012aw	1.4	379	IIP	Jerkstrand et al. (2014)
SN 2008ax	1.39	100	I Ib	Milisavljevic et al. (2010)
SN 2008ax	0.75	307	I Ib	Milisavljevic et al. (2010)
SN 2011dh	1.31	152	I Ib	Ergon et al. (2015)
SN 2011dh	0.96	272	I Ib	Ergon et al. (2015)
iPTF13bvn	1.5	290	Ib	Kuncarayakti et al. (2015)
SN 2008D	0.76	363	Ib	Tanaka et al. (2009)
SN 2013ge	0.39	159	Ib/c	Drout et al. (2016)
SN 2013ge	0.36	363	Ib/c	Drout et al. (2016)
SN 1994I	1.22	103	Ic	Filippenko et al. (1995)
SN 1994I	0.98	153	Ic	Filippenko et al. (1995)
SN 2012ap	1.78	218	Ic-bl	Milisavljevic et al. (2015b)
SN 2012ap	0.97	272	Ic-bl	Milisavljevic et al. (2015b)
SN 2002ap	0.45	185	Ic-bl	Foley et al. (2003)
SN 1998bw	0.43	376	Ic-bl	Patat et al. (2001)

Note.

^a Phase is with respect to date of discovery.

change is consistent with observations of SNe Ib/c at very evolved epochs where change is routinely negligible (Elmhamdi et al. 2004), and in line with the fact that the critical densities for [O I] and [Ca II] are comparable. Although we have not explored epochs $t > 300$ days, a decrease in the [Ca II]/[O I] ratio alone appears to be an unlikely explanation for why Ca-rich transients have strong calcium line emission.

5.2. Spectral Fingerprinting

Optical and NIR spectroscopy obtained many months to years after maximum light is a powerful probe of the kinematic and chemical properties of the ejecta closest to the explosion center. It can be used to discriminate between Type Ia versus core-collapse classifications, and even between subclassifications (Milisavljevic et al. 2012; Parrent et al. 2016a), and thus provides a unique means of spectrally fingerprinting a supernova’s progenitor system.

Few Ca-rich transients have had high-quality, multi-epoch data at late times. The close proximity and relatively slow decline rate of iPTF15eqv enabled spectroscopic observations of high signal-to-noise ratio at epochs >200 days after explosion, which is among the latest epochs ever observed for a Ca-rich transient. The high quality of the spectra reveals faint features that would be missed in lower signal-to-noise data.

We compared the day 199 spectrum of iPTF15eqv to prototypical SNe I and II (Figure 12). Spectra were arbitrarily scaled to compare and contrast the relative strengths of specific

emission features between nebular epoch spectra of iPTF15eqv and other supernovae. Clearly, iPTF15eqv and the normal, well-observed Type Ia SN 2011fe have widely different late-time emissions. Type Ia late-time spectra are dominated by a complicated blend of forbidden and permitted iron lines between 4000 and 5500 Å, many of which are associated with Fe-peak elements. Peaks centered around 7000–7600 Å associated with iron and nickel are also regularly observed. None of these features are conspicuous in iPTF15eqv.

In sharp contrast, iPTF15eqv shares many spectral signatures with core-collapse SNe. The late-time spectrum of the Type IIb SN 2011dh (Ergon et al. 2015), exhibits [O I], [Ca II], a blend of He I+Na I, a “plateau” of emission spanning 3800–5600 Å associated with Fe-peak elements, and a broad H α emission feature redward of [O I] (that may have some contribution from [N II]), which overlap with iPTF15eqv. The noticeable difference is in the strength of the Fe-peak plateau and the [Ca II]/[O I] ratio, as well as the Mg I emission, which is prominent in many SNe IIb but not so in iPTF15eqv.

A surprising similarity is also found between iPTF15eqv and SN 1998bw, which is a broad-lined Type Ic that was associated with the long-duration γ -ray burst GRB 980425 (Galama et al. 1998; Patat et al. 2001). In this case, the relative strength of the Fe-peak plateau is comparable between the two, but the [Ca II]/[O I] is much smaller. Considerable overlap between the late-time spectra of the Type IIP SN 2004et (Sahu et al. 2006) and iPTF15eqv is also evident. However, the H α line dominates the spectrum of SN 2004et ([Ca II]/H α = 0.6) and

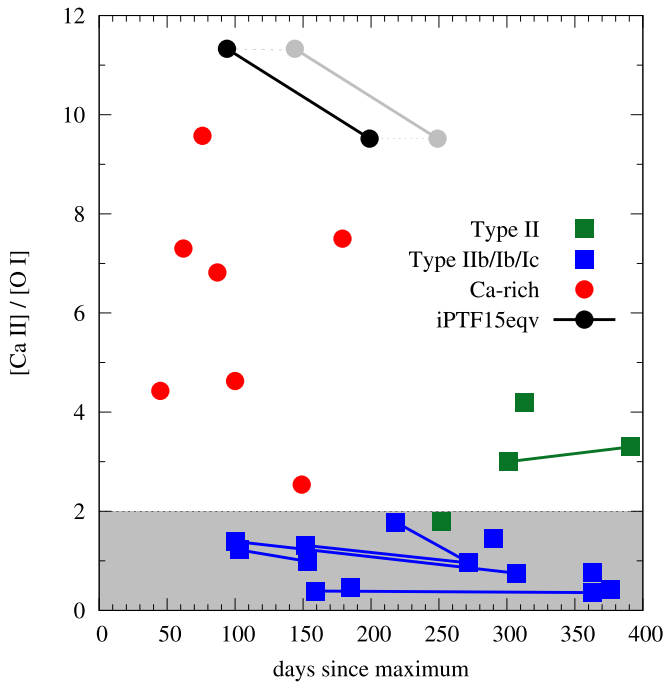


Figure 11. Ratio of [Ca II] $\lambda\lambda 7291, 7324$ to [O I] $\lambda\lambda 6300, 6364$ for Type II, Type Ib/Ib/Ic, and Ca-rich transients. At all epochs where both lines are visible and the conditions can be reasonably assessed to be nebular, all Ca-rich transients have $[\text{Ca II}]/[\text{O I}] > 2$, and all Type Ib/c are < 2 . Solid lines connect different epochs of the same object. The gray silhouette of iPTF15eqv connected by dashed lines reflects the uncertainty in the explosion date. Refer to Table 4 for the data used to create this plot.

is far stronger relative to that observed in iPTF15eqv ($[\text{Ca II}]/\text{H}\alpha = 30$; but see also Section 5.3 for a discussion of other emission lines that may contribute to this wavelength region).

Notably, the [Ca II] $\lambda\lambda 7291, 7324$ emission line profile of iPTF15eqv is unlike any other Ca-rich transient (Figures 7 and 10) and rare among SNe Ib/c. To our knowledge, the only instance is in late-time spectra of the Type Ib SN 2007uy, though in that case the velocity span was much smaller ($\lesssim 5000 \text{ km s}^{-1}$; Milisavljevic et al. 2010; Roy et al. 2013; Modjaz et al. 2014). Double-peaked profiles have been observed in the [O I] $\lambda\lambda 6300, 6364$ line profiles of SNe Ib/c and interpreted to represent ejecta asymmetry (Maeda et al. 2008; Modjaz et al. 2008; Taubenberger et al. 2009), possibly in the form of an O-rich torus (Maeda et al. 2007), which may have been shaped by a jetted explosion (Maeda et al. 2002; Mazzali et al. 2005). However, many of these cases are actually due to the doublet nature of [O I] in combination with significant density enhancements associated with ejecta clumping (Milisavljevic et al. 2010).

5.3. Hydrogen in Ca-rich Transients

The strength of the 6560 Å feature relative to [O I] observed in iPTF15eqv is broadly similar to that observed in SN 2011dh and other SNe Ib. We identify this feature to be primarily H α in iPTF15eqv; however, we have noted that Ca I $\lambda 6572$ and [N II] $\lambda\lambda 6548, 6583$ may also contribute emission in this region. In Figure 13 we show the day 199 spectrum of iPTF15eqv and a day 292 spectrum of SN 2011dh. The emission in iPTF15eqv is more narrowly peaked, which reflects differences in how the presumably H-rich ejecta are distributed in the two objects. A parabolic distribution is anticipated from a

spherical geometry. A flat-topped distribution as observed in SN 2011dh is reflective of a shell-like geometry.

iPTF15eqv is not unique in potentially exhibiting H α emission among Ca-rich transients. The subluminal and peculiar PTF09dav was reported to exhibit H α with a velocity width of $\sim 1000 \text{ km s}^{-1}$ in nebular spectra presented in Kasliwal et al. (2012). The H α emission was interpreted as circumburst material being photoionized by the interaction between the explosion and the progenitor star’s wind. The Kasliwal et al. (2012) scenario for PTF09dav is different from what we propose for iPTF15eqv, where H α exhibits higher velocities that are more easily understood as being associated with explosive ejecta. The possibility of a contribution from Ca I $\lambda 6572$ was not discussed within the context of PTF09dav. In Figure 13, we also show the Ca-rich transient PTF11kmb enlarged around the same region. Intriguingly, PTF11kmb exhibits excess emission redward of [O I] that resembles the H α distribution of SN 2011dh.

5.4. High Velocity Kicks?

To explain how Ca-rich transients explode in isolated regions devoid of massive star populations, Lyman et al. (2014) proposed long-lived progenitor systems that have been “kicked” to high velocities. Similarly, Foley (2015) argued that the progenitors of Ca-rich transients are double WD systems that have been ejected from their host galaxies after interacting with a supermassive BH. Foley (2015) analyze the nebular spectra of 13 Ca-rich transients to look for evidence in support of this hypothesis in the [Ca II] lines and find a correlation between the projected distance from the host galaxy and bulk Doppler shift velocity. Specifically, SNe with small projected offsets have large line-of-sight velocity shifts as determined by nebular lines, while those with large projected offsets have no significant velocity shifts.

We considered the implications of Foley (2015) on the unusual double-peaked [Ca II] profile of iPTF15eqv and found an important caveat in this interpretation. Although the [Ca II] line profile exhibits clear asymmetry potentially associated with a bulk Doppler shift, the profiles of all other ions of iPTF15eqv are centered near zero rest velocity (Figure 7). This characteristic of iPTF15eqv is not unique, in that the [Ca II] emission line profile of SN explosions at nebular epochs can often have an apparent blueshift attributable to internal absorption of inner ejecta (Taubenberger et al. 2009; Milisavljevic et al. 2010). If the ejecta are not completely optically thin, then emission from the rear of the expanding debris cloud is preferentially blocked. This effect, which can affect some ions more than others, gives the overall impression of being blueshifted.

We illustrate this phenomenon of apparent blueshifts in Figure 14, where we show the emission line profiles of [Ca II] and [O I] for two SNe Ib/c and two Ca-rich events, in addition to that of iPTF15eqv. [Ca II] emission has a large range distribution that sometimes reflects the same distribution as [O I] (SN 2013ge and PTF11kmb), but other times can show an apparent bulk blueshift (SN 2002ap and SN 2012hn). Foley (2015) interprets the [Ca II] profile of SN 2012hn to be associated with a systemic velocity of $-1730 \pm 70 \text{ km s}^{-1}$. However, this view is not easily reconciled with the emission line profile of [O I] that is distributed about zero velocity. Thus, we do not find strong evidence supporting a high systemic bulk

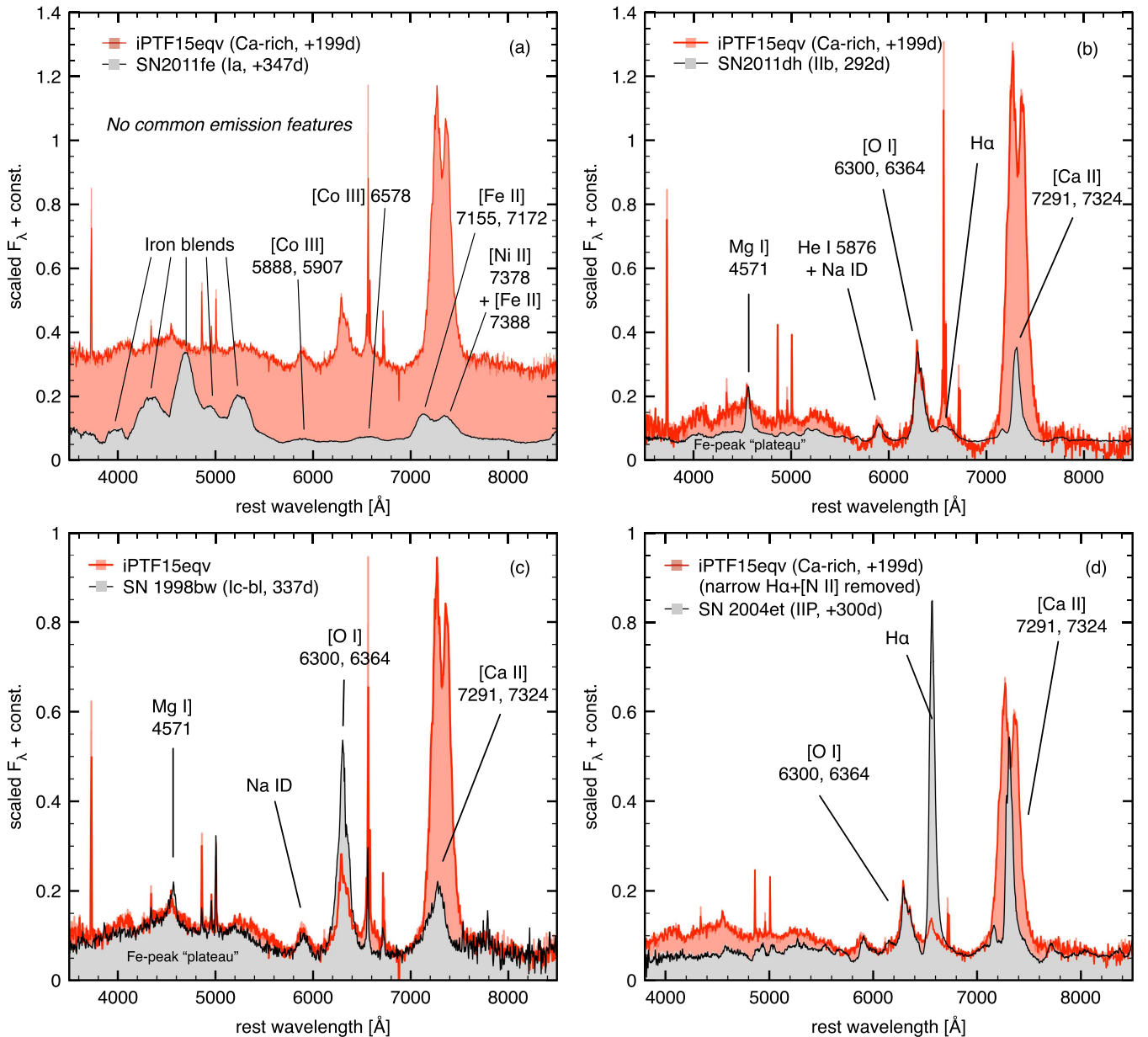


Figure 12. Spectral fingerprinting iPTF15eqv. Spectra have been arbitrarily scaled to compare and contrast the relative strengths of specific emission features between nebular epoch spectra of iPTF15eqv and other supernovae (both thermonuclear and core collapse). The spectral features of iPTF15eqv best match those of a core-collapse explosion and have little similarity to those observed in thermonuclear WD explosions. Data were originally published in Mazzali et al. (2015), Ergon et al. (2015), Patat et al. (2001), and Sahu et al. (2006).

velocity in iPTF15eqv and conclude that other Ca-rich transients may be similarly affected by optical depth effects.

Interestingly, the blueshifted [Ca II] emission of iPTF15eqv and SN 2012hn trace similar distributions. SN 2012hn, however, does not have a prominent redshifted emission peak like that observed in iPTF15eqv. This could be consistent with a shared torus geometry, if in the case of SN 2012hn its rear hemisphere has been obscured. This speculative scenario suggests that an observer’s line of sight may be an important consideration in interpreting spectra of Ca-rich transients.

5.5. Metallicities of Ca-rich Transient Host Galaxies

Although indirect lines of evidence from host galaxy samples and explosion site locations point toward low mass and low metallicity progenitor stars (Yuan et al. 2013), no

systematic observational survey of the host galaxy metallicities or explosion site SFRs of Ca-rich SNe has been conducted.

We examined five Ca-rich transients (SN 2000ds, 2001co, 2003dg, 2005E, and PTF11bij) that have host galaxies in the SDSS imaging footprint and for which we could apply the LZC relation of Sanders et al. (2013) to estimate galaxy metallicity from optical luminosity and color. The foreground-extinction-corrected absolute SDSS magnitudes for each host galaxy and the host galaxy global metallicities derived from the LZC relation on the N2 scale of Pettini & Pagel (2004) are displayed in Table 5.

Host galaxies for four of the five Ca-rich transients (SN 2000ds, 2001co, 2003dg, and PTF11bij) have $\log(\text{O}/\text{H}) + 12 \sim 8.7$, which is consistent with the metallicity reported here for iPTF15eqv. SN 2005E is the sole outlier with a substantially

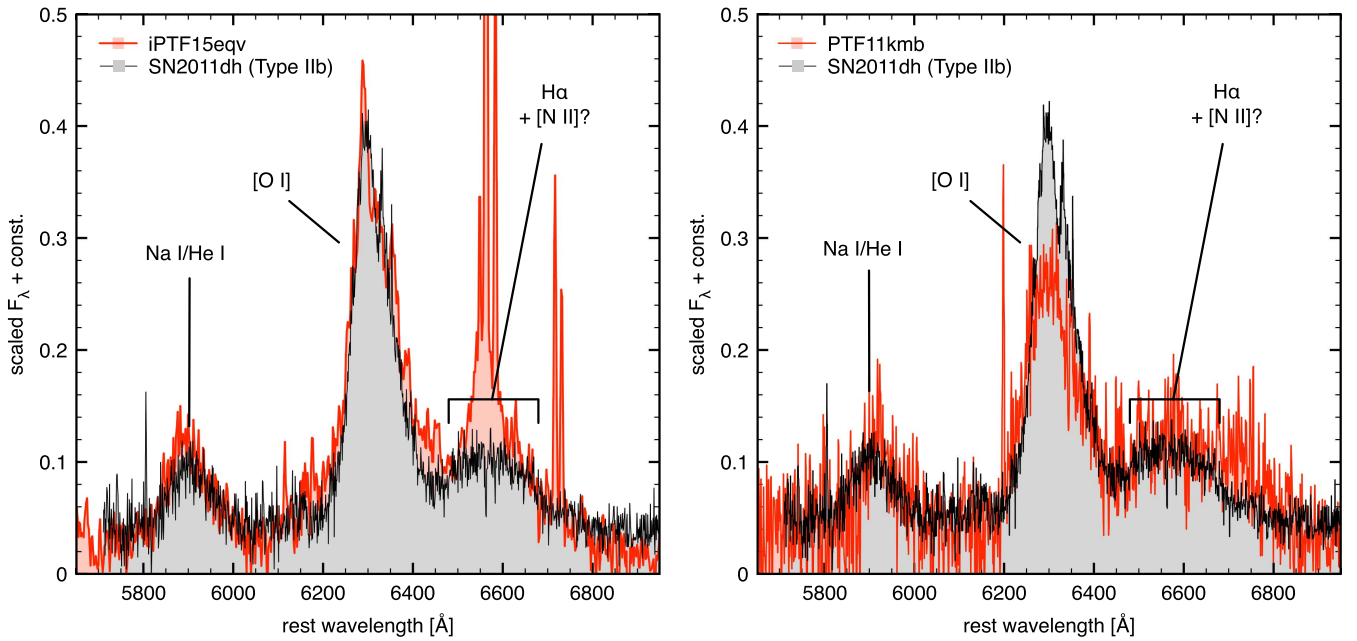


Figure 13. Optical spectra of Ca-rich transients iPTF15eqv and PTF11kmb enlarged in the region of 5800–6800 Å and scaled arbitrarily. Broad emission centered around 6560 Å is similar in distribution and strength to that observed in the Type IIb SN 2011dh (Ergon et al. 2015), where it is attributable to H α and [N II] $\lambda\lambda$ 6548, 6583. Emission from the Ca I λ 6572 line may also contribute to this feature in Ca-rich transients.

lower global metallicity ($\log(\text{O}/\text{H}) + 12 = 8.4$). Thus, we conclude that Ca-rich transients often occur in metal-rich galaxies. Notably, this finding is not at odds with a low-mass star progenitor scenario. The galaxy mass-normalized rate of SNe Ia is actually highest, marginally, in Type Sc host galaxies among all major morphological types (Li et al. 2011; see also Lyman et al. 2013).

5.6. Ca Abundance and Enrichment

The potentially large calcium abundance of Ca-rich transients, coupled with their large galactocentric distances, make them intriguing candidate drivers of chemical evolution in galaxies and the intergalactic medium (Kawabata et al. 2010; Perets et al. 2010; Kasliwal et al. 2012; Mulchaey et al. 2014). Recent works suggest that combinations of Type Ia and core-collapse nucleosynthesis models under produce the amount of calcium required by X-ray observations of the intracluster medium (de Plaa et al. 2007; Mernier et al. 2016), and that Ca-rich transients may play a role in addressing this problem (Mulchaey et al. 2014; Mernier et al. 2016). Ca-rich transients have also been invoked to explain metal-poor stars with an extremely large over-abundance of Ca, such as SDSS J234723.64+010833.4, discovered in the outer halo of our galaxy (Lai et al. 2009).

We derived O and Ca masses of $0.090^{+0.11}_{-0.08}$ and $0.006 \pm 0.002 M_{\odot}$, respectively, for iPTF15eqv from our nebular spectra. In contrast, estimates of chemical abundances of SN 2005E by Perets et al. (2010) were 0.037 and $0.135 M_{\odot}$ for O and Ca, respectively. Taking into account that the [O I] and [Ca II] emission lines of iPTF15eqv are ~ 2.5 and ~ 20 times more luminous than SN 2005E, the O abundance estimates are broadly consistent, whereas the Ca abundances are not. Some of the inconsistency may be attributable to different model assumptions, but additional discrepancies may arise from the different natures of

the explosions. Consequently, the Ca abundance yield of Ca-rich transients may vary considerably across individual events.

Regardless of the exact nucleosynthetic yields, both analyses point to a relatively large Ca/O abundance ratio, which is generally understood to be sensitive to the progenitor mass in core-collapse SNe. Models of supernova nucleosynthesis have routinely shown that larger masses of Ca are made for lower mass progenitors (Woosley & Heger 2007; Nomoto et al. 2013; Sukhbold et al. 2016). For example, theoretical models predict that stars having main-sequence masses of $13 M_{\odot}$ and $18 M_{\odot}$ produce Ca/O ratios (by mass) of 0.025 and 0.005, respectively (Nomoto et al. 2013). Keeping with this trend, in order to produce a relatively large Ca/O ratio of ≈ 0.07 observed in iPTF15eqv, the mass of its progenitor star would have been $< 13 M_{\odot}$ and thus approach the threshold for core collapse ($8 \pm 1 M_{\odot}$; Smartt 2009).

5.7. Electron Capture Supernova?

Stars in the mass range $8\text{--}12 M_{\odot}$ can exhibit structural peculiarities during their evolution that considerably affect the supernova explosion dynamics if they undergo core collapse. Electron captures on ^{24}Mg and ^{20}Ne in a degenerate O–Ne–Mg core of mass $\sim 1.37 M_{\odot}$ can drive the core toward collapse in what is referred to as an “electron-capture supernova” (ECSN; Nomoto 1984). This progenitor scenario was invoked to explain the Ca-rich SN 2005cz (Kawabata et al. 2010). The winds of such stars are not strong enough to remove hydrogen envelopes, which led Kawabata et al. (2010) to suggest that binary interaction via Roche-lobe overflow or common envelope ejection could explain why no conspicuous hydrogen was present in their optical spectra of SN 2005cz. A similar progenitor scenario could apply to iPTF15eqv.

Generally, numerical simulations of ECSNe explode with kinetic energies of $\sim 10^{50}$ erg and synthesize $\sim 10^{-3} M_{\odot}$ of radioactive ^{56}Ni (e.g., Kitaura et al. 2006). These values are each approximately an order of magnitude less than those we

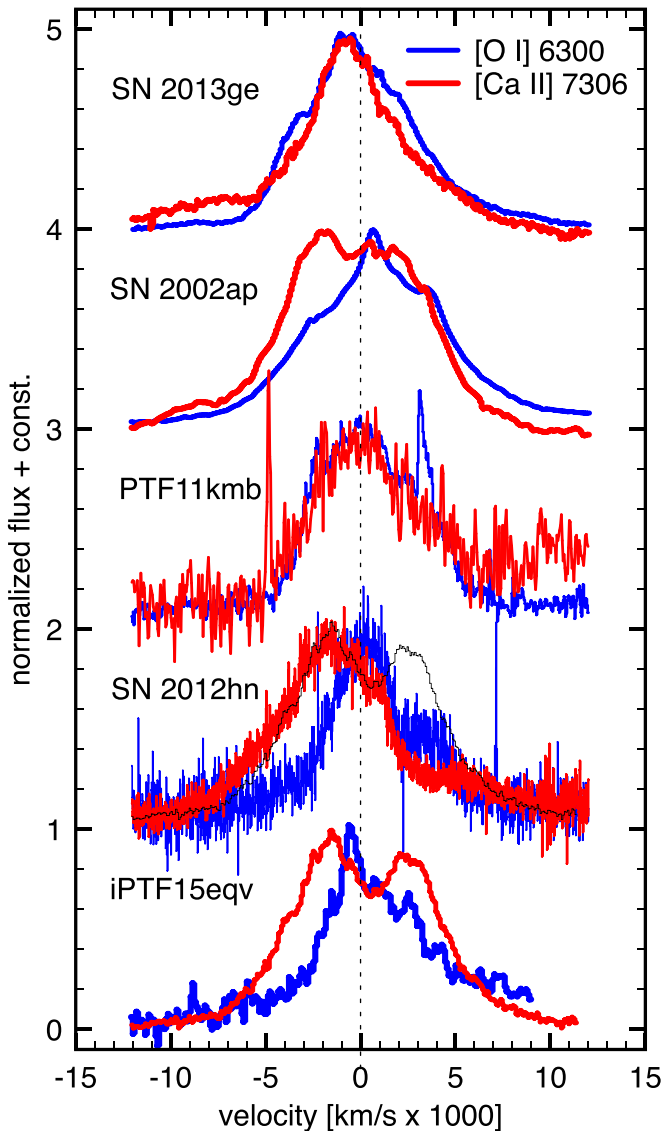


Figure 14. Emission line profiles of [O I] $\lambda\lambda 6300, 6364$ and [Ca II] $\lambda\lambda 7291, 7324$ for SNe Ib/c and Ca-rich transients. Velocities are with respect to 6300 \AA and 7306 \AA , respectively. The [Ca II] profile does not always overlap with [O I], which makes it a poor tracer of the systemic velocity of bulk ejecta. Data were obtained from WISEREP and the OSC and were originally published in the following papers: SN 2013ge (Drout et al. 2016), SN 2002ap (Foley et al. 2003), PTF11kmb (Kasliwal et al. 2012), SN 2012hn (Valenti et al. 2014), and iPTF15eqv (this paper).

infer for iPTF15eqv (Section 4.1). However, there are many uncertainties with the explosion processes of ECSNe (see, e.g., Jones et al. 2013; Woosley & Heger 2015). Perhaps the strongest signature of an ECSN is that it likely leaves behind a very special abundance pattern in its ejecta (see the recent review by Müller 2016), which may be abundant in isotopes of calcium (Wanajo et al. 2013).

Moriya & Eldridge (2016) investigated the expected rates and bolometric light curve properties of stripped-envelope ECSNe using stellar models from the Binary Population and Spectral Synthesis (BPASS) code¹⁸ (Eldridge et al. 2008, 2011; Stanway et al. 2016). We compared the light curve of iPTF15eqv to the Type IIb, $Z = 0.020$ models and were

unable to find a strict match. However, the Moriya & Eldridge (2016) models are fixed at $2.5 \times 10^{-3} M_{\odot}$ of ^{56}Ni , which mainly changes the peak luminosity. By scaling the luminosity of a model having a total ejecta mass of $1.5 M_{\odot}$ and hydrogen envelope mass of $0.35 M_{\odot}$, reasonable agreement is possible if M_{Ni} is allowed to range between 0.045 and $0.055 M_{\odot}$ (Figure 15). The range in mass of our fit is due to the uncertainty in the explosion date. These results are consistent with our independent derivation of M_{Ni} in Section 4.1.

Notably, binary systems of stars in the mass range that develop to ECSNe can significantly extend the delay-time distribution of core-collapse SNe. For single stars, the maximum lifetime is approximately ~ 50 Myr. However, the majority of binary progenitors in the Moriya & Eldridge (2016) models have lifetimes of 30–100 Myr, and the oldest lifetime is 200 Myr. A population synthesis study conducted by Zapartas et al. (2017) to compute the delay-time distribution of core-collapse SNe also found that a significant fraction can occur 50–200 Myr after birth, well after all massive single stars have already exploded. These late events originate mostly from binary systems with both stars of mass $4\text{--}8 M_{\odot}$.

5.8. Ultra-stripped Supernova?

Ultra-stripped SNe are core-collapse SNe whose ejecta masses are only $\sim 0.1 M_{\odot}$ (Tauris et al. 2013, 2015). The small ejecta masses result from the extreme stripping of their progenitors due to the existence of compact companion stars (Tauris et al. 2013, 2015). The ultra-stripped SNe are found to explode successfully with the neutrino-driven mechanism, with explosion energies of $\sim 10^{50}$ erg and ^{56}Ni masses of $\sim 0.01 M_{\odot}$ (Suwa et al. 2015). Moriya et al. (2017) found that light curves and spectra of some Ca-rich transients match well to those predicted by ultra-stripped SNe, suggesting some Ca-rich transients may be ultra-stripped SNe.

Ultra-stripped SN light curve models currently available tend to decline faster than that of iPTF15eqv (Tauris et al. 2013; Moriya et al. 2017). However, the current light curve models are only available for progenitors with ejecta masses below $0.2 M_{\odot}$ (Tauris et al. 2013; Moriya et al. 2017). There exist ultra-stripped SNe with larger ejecta masses (Tauris et al. 2015), and they can have slower decline rates, possibly matching iPTF15eqv. One problem applying the ultra-stripped model to iPTF15eqv is that iPTF15eqv likely exhibits hydrogen in our late-time spectra (Sections 4.2 and 5.3; Figure 13). Ultra-stripped SN progenitors lack hydrogen because of the extreme stripping, and their companions are compact stars that do not have hydrogen. Therefore, no hydrogen is expected to exist in the progenitor system. We consider an ultra-stripped SN origin unlikely for iPTF15eqv, although further work on this progenitor scenario is needed.

5.9. Mass-loss Environment

Mass loss is a key process in stellar evolution, and thus is a powerful probe of the progenitor systems of SNe (Puls et al. 2008; Smith 2014). Observations of SNe at radio and X-ray wavelengths can reconstruct the mass-loss history of its progenitor system as the SN blast wave passes through and interacts with surrounding material (Chevalier 1982, 1998). To date, no SN Ia has been detected at X-ray or radio wavelengths (Margutti et al. 2012, 2014; Chomiuk et al. 2016), suggesting a relatively clean environment with densities below $n < 3 \text{ cm}^{-3}$

¹⁸ <http://bpass.auckland.ac.nz>

Table 5
Host Galaxy Properties of Ca-rich Transients

SN	Host Galaxy	z	M_g	M_r	$\log(\text{O}/\text{H}) + 12$ (LZC; PP04 N2)
2000ds	NGC 2768	0.0045	-20.09	-21.00	8.71
2001co	NGC 5559	0.0172	-20.02	-20.69	8.71
2003dg	UGC 6934	0.0183	-19.46	-20.13	8.70
2005E	NGC 1032	0.0090	-19.69	-21.07	8.41
PTF11bij	IC 3956	0.0347	-20.49	-21.27	8.72
iPTF15eqv	NGC 3430	0.0053	-19.50	-20.08	8.67

Note. Photometries are SDSS DR12 cModel magnitudes (Alam et al. 2015) extinction-corrected for the Galaxy foreground (Schlafly & Finkbeiner 2011). The oxygen abundances were derived using the LZC relation of Sanders et al. (2013) using g' and r' photometry and standardizing on the N2 diagnostic scale of Pettini & Pagel (2004).

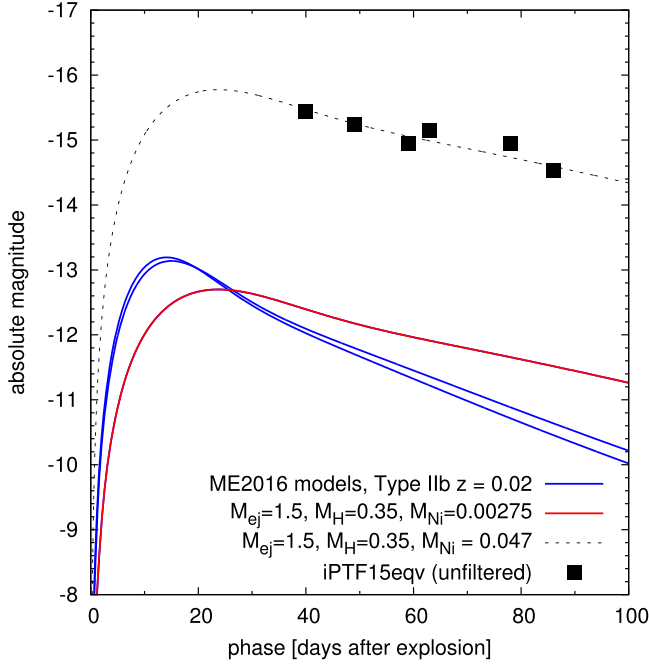


Figure 15. Light curve of iPTF15eqv compared to bolometric light curves from models of ECSNe in close binary systems presented in Moriya & Eldridge (2016). These models are for Type IIb explosions with $Z = 0.02$, and progenitors with $0.35 M_{\odot}$ of hydrogen at the time of explosion. We find reasonable consistency between iPTF15eqv and a model having a total ejecta mass of $1.5 M_{\odot}$ if we scale the luminosity to mimic $0.047 M_{\odot}$ of nickel.

at $R \sim 10^{16}$ cm and progenitor system mass-loss rates of $\dot{M} < 10^{-9} \frac{M_{\odot}}{\text{yr}} \frac{100 \text{ km s}^{-1}}{\text{km s}^{-1}}$. In contrast, core-collapse SNe exhibit a wide range of X-ray and radio properties that reflect the diversity of their environments that have been sculpted by the progenitor system's mass loss (Weiler et al. 2002; Kotak & Vink 2006; Soderberg et al. 2006; Chevalier & Soderberg 2010; Wellons et al. 2012; Margutti et al. 2013, 2017).

Chomiuk et al. (2016) examined radio upper limits for Ca-rich transients in the context of Type Ia thermonuclear WD explosions. Assuming a total ejecta mass of $0.3 M_{\odot}$ and kinetic energy of 4×10^{50} erg, they constrain $\dot{M} < 10^{-5} M_{\odot} \text{ yr}^{-1}$ for $v_w = 100 \text{ km s}^{-1}$ for most objects of their sample. This allows them to rule out the presence of tidal tails (Raskin & Kasen 2013), in the case where stripping of the He WD occurred a few years before SN explosion, as well as the presence of strong accretion-powered outflows or winds (Hachisu et al. 1999), as might be expected if a disrupted WD is accreted.

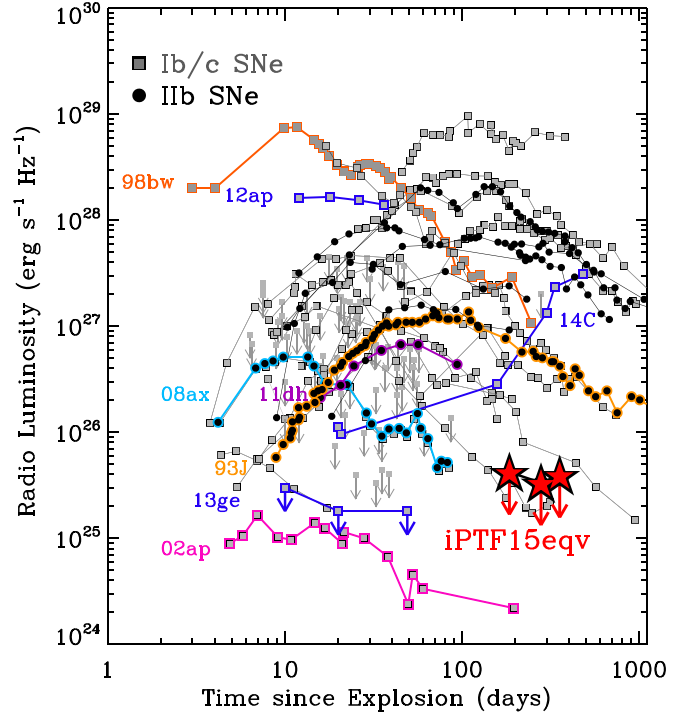


Figure 16. Upper limits on radio emission from iPTF15eqv compared to the radio light curves of SNe IIb and Ib/c. Data were originally published in Margutti et al. (2013) and references therein, Milisavljevic et al. (2013a) and references therein, Bufano et al. (2014), Kamble et al. (2016, 2014), Drout et al. (2016), and Margutti et al. (2017).

In light of the overlap in properties between iPTF15eqv and core-collapse SNe (Section 5.2), we compared our VLA upper limits on radio emission from iPTF15eqv to the radio light curves of SNe IIb and Ib/c (Figure 16). Our observations rule out environments similar to those observed around the Type IIb SN 1993J and SN 2011dh, which exhibited radio light curves that are more luminous than iPTF15eqv and were estimated to have mass-loss rates ranging between $\dot{M} \approx 2.4 \times 10^{-5} M_{\odot} \text{ yr}^{-1}$ ($v_w = 10 \text{ km s}^{-1}$) and $\dot{M} \approx 6 \times 10^{-5} M_{\odot} \text{ yr}^{-1}$ ($v_w = 1000 \text{ km s}^{-1}$), respectively. The environments of other Type IIb such as SN 2008ax with $\dot{M} = (9 \pm 3) \times 10^{-6} M_{\odot} \text{ yr}^{-1}$ (for $v_w = 10 \text{ km s}^{-1}$) are not ruled out (Roming et al. 2009). The difference in mass-loss rates of SNe IIb may reflect the size and evolutionary status of the progenitor star (Chevalier & Soderberg 2010; Kamble et al. 2016). Many SNe Ib/c such as SN 2013ge (Drout et al. 2016) and SN 2002ap (Berger et al. 2002) with relatively clean environments are not

ruled out, but late-interacting SNe Ib/c such as SN 2014C are ruled out (Milisavljevic et al. 2015a; Margutti et al. 2017).

Our deep non-detections up to ~ 400 days imply a low-density environment ($n \lesssim 0.1 \text{ cm}^{-3}$) for the progenitor of iPTF15eqv out to $R \sim 10^{17} \text{ cm}$. Using a typical forward shock velocity of $\approx 3 \times 10^4 \text{ km s}^{-1}$ for core-collapse SNe, we estimate that the progenitor system of iPTF15eqv did not undergo any enhanced mass loss or eruptive activity within $\sim 300\text{--}1000$ ($v_w/100 \text{ km s}^{-1}$) years of the SN.

6. Conclusions

We have presented multiwavelength observations and analysis of the supernova explosion iPTF15eqv in NGC 3430. We find that iPTF15eqv has a combination of properties that bridge those observed in Ca-rich transients and SNe Ib/c. Perhaps most revealing about iPTF15eqv is its large $[\text{Ca II}]/[\text{O I}] \approx 10$ emission line ratio, which is among the highest encountered among Ca-rich events, and clear Type Ib/c and Type II spectroscopic signatures (Figure 12) seen in our optical and NIR data $\gtrsim 200$ days post-explosion. This discovery is significant because discussions of SNe Ia often include Ca-rich transients (e.g., Parrent et al. 2014; Chomiuk et al. 2016), and our work establishes that an unknown percentage of SNe that have been considered to be Ca-rich transients may be associated with massive star explosions.

Our data allow us to place many constraints on the chemical abundance yields of the explosion and the nature of the progenitor system of iPTF15eqv:

1. We estimate $M_{\text{ej}} \approx 2\text{--}4 M_{\odot}$, $M_{\text{Ni}} \approx 0.04\text{--}0.07 M_{\odot}$, and $E_k \approx (0.8\text{--}2) \times 10^{51} \text{ erg}$, assuming an explosion date sometime between 2015 July 24 and September 12.
2. We derive an O:Ca abundance ratio (by number) of 39 ± 24 , S:Ca abundance ratio of 29 ± 7 , and Si:S abundance ratio of ~ 1 .
3. Upper limits on possible radio emission from iPTF15eqv made with the VLA suggest a low-density environment ($n \lesssim 0.1 \text{ cm}^{-3}$) within a radius of $\sim 10^{17} \text{ cm}$ of the explosion site.
4. We do not observe X-ray emission that would be associated with accretion onto a BH to an upper limit of $5.3 \times 10^{38} \text{ erg s}^{-1}$, which constrains the possibility of any BH to a mass $\lesssim 100 M_{\odot}$.
5. The leading candidate progenitor system is a H-poor star of mass $\lesssim 10 M_{\odot}$ that interacted with a nearby companion star. The chemical abundances and ejecta kinematics inferred from our late-time spectra suggest that the explosion may have been an ECSN.

iPTF15eqv forces a sober reconsideration of its “Ca-rich transient” classification. On the one hand, without early epoch photometry and spectra to constrain its light curve and specific SN classification, iPTF15eqv does not strictly fit the criteria of a “SN 2005E-like” (Perets et al. 2010) or “Ca-rich gap transient” (Kasliwal et al. 2012). However, iPTF15eqv does exhibit strong calcium line emission seen in other SNe having incomplete spectral and photometric characterization (including 2003H, 2003dr, 2003dg, 2001co, 2000ds) that have been investigated as Ca-rich transients. It is noteworthy that objects considered to be Ca-rich transients thus far all share spectral evolution that truly distinguishes them from other SNe (see Figures 10 and 11), which is an indication that the observational classification is meaningful.

As data improve in quality and wavelength span (particularly in the NIR; see Section 4.2) the ability to define a further subdivision in the class may be achievable, as was done in the Type I classification of Minkowski (1941) that was later split to Type Ia (thermonuclear explosions of WDs) and Type Ib/c (massive star core collapses). However, reconciling how two radically different progenitor channels can exhibit similar emission properties at nebular epochs when emission is from interior ejecta will be challenging (Figure 12).











The relatively long delay-time distribution and distinguishable abundance patterns of ECSNe from binary systems make them an attractive progenitor system for at least some Ca-rich transients. It is important to note, however, that alternative models not immediately applicable to iPTF15eqv, including “ultra-stripped” SNe and violent disruptions of WDs, successfully reproduce other observed properties of Ca-rich transients. Additional theoretical work that can provide distinct signatures of the various progenitor scenarios is needed.

In the case of iPTF15eqv, high-resolution imaging obtained after the SN has faded can map out the surrounding stellar environment and be used to investigate whether a massive star association is nearby. More generally, NIR spectra at nebular epochs proved to be critical for our line identifications and diagnostics, and it is hoped that future Ca-rich transients can be observed and analyzed in this way. Perhaps the most pertinent issue for Ca-rich transients is to quantify their calcium abundances more accurately. Given that present estimates of their yields vary across orders of magnitude, more stringent constraints on their progenitor systems and improved models of their late-time emissions are needed if a precise understanding of the chemical enrichment of galaxies and the intracluster medium is to be achieved.

We thank the referee H. Perets for a critical reading of our manuscript and for providing many suggestions that improved its content and presentation. Observations reported here were obtained at the MMT Observatory, a joint facility of the Smithsonian Institution and the University of Arizona. Based on observations made by the *Chandra X-ray Observatory* under program GO 16500534, PI Margutti, observations ID 16821. The National Radio Astronomy Observatory is a facility of the National Science Foundation operated under cooperative agreement by Associated Universities, Inc. This paper made use of the Weizmann interactive supernova data repository (WISEREP)—<http://wiserep.weizmann.ac.il>—and the Open Supernova Catalog—<http://sne.space>. K. Kawabata kindly provided data of SN 2005cz. T.J.M. is supported by the Grant-in-Aid for Research Activity Start-up of the Japan Society for the Promotion of Science (16H07413). R.M. gratefully acknowledges support from the Research Corporation for Science Advancement. The authors acknowledge the Telescope Data Center of the Smithsonian Astrophysical Observatory for performing MMIRS data reduction. I.C. acknowledges partial support by the Russian French PICS International Laboratory program (No. 6590) co-funded by the RFBR (project 15-52-15050), by the RFBR project 15-32-21062, and the presidential grant MD-7355.2015.2. This work is based in part on observations obtained at the MDM Observatory, operated by Dartmouth College, Columbia University, Ohio State University, Ohio University, and the University of Michigan.

Facilities: MMT (Blue Channel spectrograph, MMTcam, MMIRS), Hiltner (OSMOS), EVLA, CXO.

ORCID iDs

Dan Milisavljevic  <https://orcid.org/0000-0002-0763-3885>
 Daniel J. Patnaude  <https://orcid.org/0000-0002-7507-8115>
 John C. Raymond  <https://orcid.org/0000-0002-7868-1622>
 Raffaella Margutti  <https://orcid.org/0000-0003-4768-7586>
 Atish Kamble  <https://orcid.org/0000-0003-0861-5168>
 James Guillochon  <https://orcid.org/0000-0002-9809-8215>
 Jerod T. Parrent  <https://orcid.org/0000-0002-5103-7706>
 Igor V. Chilingarian  <https://orcid.org/0000-0002-7924-3253>
 Matthew T. Penny  <https://orcid.org/0000-0001-7506-5640>
 Takashi J. Moriya  <https://orcid.org/0000-0003-1169-1954>

References

- Alam, S., Albareti, F. D., Allende Prieto, C., et al. 2015, *ApJS*, **219**, 12
 Arnett, W. D. 1982, *ApJ*, **253**, 785
 Berger, E., Kulkarni, S. R., & Chevalier, R. A. 2002, *ApJL*, **577**, L5
 Bersten, M. C., Benvenuto, O. G., Nomoto, K., et al. 2012, *ApJ*, **757**, 31
 Bufano, F., Pignata, G., Bersten, M., et al. 2014, *MNRAS*, **439**, 1807
 Cao, Y., Kulkarni, S. R., Cook, D., & Vreeswijk, P. 2015, *ATel*, **8428**
 Chevalier, R. A. 1982, *ApJ*, **259**, 302
 Chevalier, R. A. 1998, *ApJ*, **499**, 810
 Chevalier, R. A., & Fransson, C. 2006, *ApJ*, **651**, 381
 Chevalier, R. A., & Soderberg, A. M. 2010, *ApJL*, **711**, L40
 Chilingarian, I., Beletsky, Y., Moran, S., et al. 2015, *PASP*, **127**, 406
 Chomiuk, L., Soderberg, A. M., Chevalier, R. A., et al. 2016, *ApJ*, **821**, 119
 Clocchiatti, A., Wheeler, J. C., Phillips, M. M., et al. 1997, *ApJ*, **483**, 675
 de Plaa, J., Werner, N., Bleeker, A. A. M., et al. 2007, *A&A*, **465**, 345
 de Vaucouleurs, G., de Vaucouleurs, A., Corwin, H. G., Jr., et al. 1991, Third Reference Catalogue of Bright Galaxies (Berlin: Springer)
 Del Zanna, G., Dere, K. P., Young, P. R., Landi, E., & Mason, H. E. 2015, *A&A*, **582**, A56
 Dessart, L., & Hillier, D. J. 2015, *MNRAS*, **447**, 1370
 Drout, M. R., Milisavljevic, D., Parrent, J., et al. 2016, *ApJ*, **821**, 57
 Drout, M. R., Soderberg, A. M., Gal-Yam, A., et al. 2011, *ApJ*, **741**, 97
 Eldridge, J. J., Izzard, R. G., & Tout, C. A. 2008, *MNRAS*, **384**, 1109
 Eldridge, J. J., Langer, N., & Tout, C. A. 2011, *MNRAS*, **414**, 3501
 Elmhamdi, A., Danziger, I. J., Branch, D., et al. 2006, *A&A*, **450**, 305
 Elmhamdi, A., Danziger, I. J., Cappellaro, E., et al. 2004, *A&A*, **426**, 963
 Ergon, M., Jerkstrand, A., Sollerman, J., et al. 2015, *A&A*, **580**, A142
 Fernández, R., & Metzger, B. D. 2013, *ApJ*, **763**, 108
 Filippenko, A. V. 1997, *ARA&A*, **35**, 309
 Filippenko, A. V., Barth, A. J., Matheson, T., et al. 1995, *ApJL*, **450**, L11
 Filippenko, A. V., Chornock, R., Swift, B., et al. 2003, *IAUC*, **8159**, 2
 Filippenko, A. V., Foley, R. J., Chornock, R., & Matheson, T. 2004, *IAUC*, **8420**, 2
 Foley, R. J. 2015, *MNRAS*, **452**, 2463
 Foley, R. J., Papenkova, M. S., Swift, B. J., et al. 2003, *PASP*, **115**, 1220
 Fransson, C., & Chevalier, R. A. 1989, *ApJ*, **343**, 323
 Galama, T. J., Vreeswijk, P. M., van Paradijs, J., et al. 1998, *Natur*, **395**, 670
 Gal-Yam, A. 2016, arXiv:1611.09353
 Guillochon, J., Parrent, J., & Margutti, R. 2017, *ApJ*, **835**, 64
 Guillochon, J., & Ramirez-Ruiz, E. 2013, *ApJ*, **767**, 25
 Gvarnadze, V. V., Langer, N., Fossati, L., et al. 2017, *NatAs*, **1**, 0116
 Hachisu, I., Kato, M., & Nomoto, K. 1999, *ApJ*, **522**, 487
 Hamuy, M., Walker, A. R., Suntzeff, N. B., et al. 1992, *PASP*, **104**, 533
 Jerkstrand, A., Ergon, M., Smartt, S. J., et al. 2015, *A&A*, **573**, A12
 Jerkstrand, A., Smartt, S. J., Fraser, M., et al. 2014, *MNRAS*, **439**, 3694
 Jones, S., Hirschi, R., Nomoto, K., et al. 2013, *ApJ*, **772**, 150
 Kalberla, P. M. W., Burton, W. B., Hartmann, D., et al. 2005, *A&A*, **440**, 775
 Kamble, A., Margutti, R., Soderberg, A. M., et al. 2016, *ApJ*, **818**, 111
 Kamble, A., Soderberg, A. M., Chomiuk, L., et al. 2014, *ApJ*, **797**, 2
 Kasliwal, M. M., Kulkarni, S. R., Gal-Yam, A., et al. 2012, *ApJ*, **755**, 161
 Kawabata, K. S., Maeda, K., Nomoto, K., et al. 2010, *Natur*, **465**, 326
 Kewley, L. J., & Dopita, M. A. 2002, *ApJS*, **142**, 35
 Kewley, L. J., & Ellison, S. L. 2008, *ApJ*, **681**, 1183
 Kewley, L. J., Geller, M. J., & Jansen, R. A. 2004, *AJ*, **127**, 2002
 Kitaura, F. S., Janka, H.-T., & Hillebrandt, W. 2006, *A&A*, **450**, 345
 Kotak, R., & Vink, J. S. 2006, *A&A*, **460**, L5
 Kuncarayakti, H., Maeda, K., Bersten, M. C., et al. 2015, *A&A*, **579**, A95
 Lagattuta, D. J., Mould, J. R., Staveley-Smith, L., et al. 2013, *ApJ*, **771**, 88
 Lai, D. K., Rockosi, C. M., Bolte, M., et al. 2009, *ApJL*, **697**, L63
 Landi, E., Young, P. R., Dere, K. P., Del Zanna, G., & Mason, H. E. 2013, *ApJ*, **763**, 86
 Leonard, D. C., Filippenko, A. V., Gates, E. L., et al. 2002, *PASP*, **114**, 35
 Li, W., Chornock, R., Leaman, J., et al. 2011, *MNRAS*, **412**, 1473
 Lunnan, R., Kasliwal, M. M., Cao, Y., et al. 2017, *ApJ*, **836**, 60
 Lyman, J. D., James, P. A., Perets, H. B., et al. 2013, *MNRAS*, **434**, 527
 Lyman, J. D., Levan, A. J., Church, R. P., Davies, M. B., & Tanvir, N. R. 2014, *MNRAS*, **444**, 2157
 Lyman, J. D., Levan, A. J., James, P. A., et al. 2016, *MNRAS*, **458**, 1768
 MacLeod, M., Goldstein, J., Ramirez-Ruiz, E., Guillochon, J., & Samsing, J. 2014, *ApJ*, **794**, 9
 MacLeod, M., Guillochon, J., Ramirez-Ruiz, E., Kasen, D., & Rosswog, S. 2016, *ApJ*, **819**, 3
 Maeda, K., Kawabata, K., Mazzali, P. A., et al. 2008, *Sci*, **319**, 1220
 Maeda, K., Nakamura, T., Nomoto, K., et al. 2002, *ApJ*, **565**, 405
 Maeda, K., Tanaka, M., Nomoto, K., et al. 2007, *ApJ*, **666**, 1069
 Margalit, B., & Metzger, B. D. 2016, *MNRAS*, **461**, 1154
 Margutti, R., Kamble, A., Milisavljevic, D., et al. 2017, *ApJ*, **835**, 140
 Margutti, R., Parrent, J., Kamble, A., et al. 2014, *ApJ*, **790**, 52
 Margutti, R., Soderberg, A. M., Chomiuk, L., et al. 2012, *ApJ*, **751**, 134
 Margutti, R., Soderberg, A. M., Wieringa, M. H., et al. 2013, *ApJ*, **778**, 18
 Martini, P., Stoll, R., Derwent, M. A., et al. 2011, *PASP*, **123**, 187
 Mazzali, P. A., Kawabata, K. S., Maeda, K., et al. 2005, *Sci*, **308**, 1284
 Mazzali, P. A., Sullivan, M., Filippenko, A. V., et al. 2015, *MNRAS*, **450**, 2631
 McLeod, B., Fabricant, D., Nystrom, G., et al. 2012, *PASP*, **124**, 1318
 Meng, X., & Han, Z. 2015, *A&A*, **573**, A57
 Mernier, F., de Plaa, J., Pinto, C., et al. 2016, *A&A*, **595**, A126
 Metzger, B. D. 2012, *MNRAS*, **419**, 827
 Milisavljevic, D., Fesen, R. A., Chevalier, R. A., et al. 2012, *ApJ*, **751**, 25
 Milisavljevic, D., Fesen, R. A., Gerardy, C. L., Kirshner, R. P., & Challis, P. 2010, *ApJ*, **709**, 1343
 Milisavljevic, D., Margutti, R., Kamble, A., et al. 2015a, *ApJ*, **815**, 120
 Milisavljevic, D., Margutti, R., Parrent, J. T., et al. 2015b, *ApJ*, **799**, 51
 Milisavljevic, D., Margutti, R., Soderberg, A. M., et al. 2013a, *ApJ*, **767**, 71
 Milisavljevic, D., Soderberg, A. M., Margutti, R., et al. 2013b, *ApJL*, **770**, L38
 Minkowski, R. 1941, *PASP*, **53**, 224
 Modjaz, M., Blondin, S., Kirshner, R. P., et al. 2014, *AJ*, **147**, 99
 Modjaz, M., Kirshner, R. P., Blondin, S., Challis, P., & Matheson, T. 2008, *ApJL*, **687**, L9
 Moriya, T. J., & Eldridge, J. J. 2016, *MNRAS*, **461**, 2155
 Moriya, T. J., Mazzali, P. A., Tominaga, N., et al. 2017, *MNRAS*, **466**, 2085
 Moustakas, J., Kennicutt, R. C., Jr., & Tremonti, C. A. 2006, *ApJ*, **642**, 775
 Mulchaey, J. S., Kasliwal, M. M., & Kollmeier, J. A. 2014, *ApJL*, **780**, L34
 Müller, B. 2016, *PASA*, **33**, 48
 Nakano, S., Itagaki, K., & Kadota, K. 2004, *IAUC*, **8419**, 2
 Nomoto, K. 1984, *ApJ*, **277**, 791
 Nomoto, K., Kobayashi, C., & Tominaga, N. 2013, *ARA&A*, **51**, 457
 Oke, J. B. 1990, *AJ*, **99**, 1621
 Parrent, J., Friesen, B., & Parthasarathy, M. 2014, *Ap&SS*, **351**, 1
 Parrent, J. T., Howell, D. A., Fesen, R. A., et al. 2016a, *MNRAS*, **457**, 3702
 Parrent, J. T., Milisavljevic, D., Soderberg, A. M., & Parthasarathy, M. 2016b, *ApJ*, **820**, 75
 Patat, F., Cappellaro, E., Danziger, J., et al. 2001, *ApJ*, **555**, 900
 Perets, H. B. 2014, arXiv:1407.2254
 Perets, H. B., Gal-Yam, A., Crockett, R. M., et al. 2011, *ApJL*, **728**, L36
 Perets, H. B., Gal-Yam, A., Mazzali, P. A., et al. 2010, *Natur*, **465**, 322
 Perets, H. B., Li, Z., Lombardi, J. C., Jr., & Milcarek, S. R., Jr. 2016, *ApJ*, **823**, 113
 Pettini, M., & Pagel, B. E. J. 2004, *MNRAS*, **348**, L59
 Pindzola, M. S., Bhatia, A. K., & Temkin, A. 1977, *PhRvA*, **15**, 35
 Puls, J., Vink, J. S., & Najarro, F. 2008, *A&Ar*, **16**, 209
 Raskin, C., & Kasen, D. 2013, *ApJ*, **772**, 1
 Rees, M. J. 1988, *Natur*, **333**, 523
 Roming, P. W. A., Pritchard, T. A., Brown, P. J., et al. 2009, *ApJL*, **704**, L118
 Rosswog, S., Ramirez-Ruiz, E., & Hix, W. R. 2008, *ApJ*, **679**, 1385
 Roy, R., Kumar, B., Maund, J. R., et al. 2013, *MNRAS*, **434**, 2032
 Sahu, D. K., Anupama, G. C., Srividya, S., & Muneer, S. 2006, *MNRAS*, **372**, 1315
 Samson, A. M., & Berrington, K. A. 2001, *ADNDT*, **77**, 87
 Sanders, N. E., Caldwell, N., McDowell, J., & Harding, P. 2012a, *ApJ*, **758**, 133
 Sanders, N. E., Levesque, E. M., & Soderberg, A. M. 2013, *ApJ*, **775**, 125
 Sanders, N. E., Soderberg, A. M., Levesque, E. M., et al. 2012b, *ApJ*, **758**, 132
 Schlafly, E. F., & Finkbeiner, D. P. 2011, *ApJ*, **737**, 103
 Schmidt, G. D., Weymann, R. J., & Foltz, C. B. 1989, *PASP*, **101**, 713

- Sell, P. H., Maccarone, T. J., Kotak, R., Knigge, C., & Sand, D. J. 2015, [MNRAS](#), **450**, 4198
- Shen, K. J., & Bildsten, L. 2009, [ApJ](#), **699**, 1365
- Shen, K. J., Kasen, D., Weinberg, N. N., Bildsten, L., & Scannapieco, E. 2010, [ApJ](#), **715**, 767
- Smartt, S. J. 2009, [ARA&A](#), **47**, 63
- Smith, N. 2014, [ARA&A](#), **52**, 487
- Soderberg, A. M., Chevalier, R. A., Kulkarni, S. R., & Frail, D. A. 2006, [ApJ](#), **651**, 1005
- Sorce, J. G., Tully, R. B., Courtois, H. M., et al. 2014, [MNRAS](#), **444**, 527
- Spyromilio, J. 1994, [MNRAS](#), **266**, L61
- Stanway, E. R., Eldridge, J. J., & Becker, G. D. 2016, [MNRAS](#), **456**, 485
- Suh, H., Yoon, S.-c., Jeong, H., & Yi, S. K. 2011, [ApJ](#), **730**, 110
- Sukhbold, T., Ertl, T., Woosley, S. E., Brown, J. M., & Janka, H.-T. 2016, [ApJ](#), **821**, 38
- Suwa, Y., Yoshida, T., Shibata, M., Umeda, H., & Takahashi, K. 2015, [MNRAS](#), **454**, 3073
- Tanaka, M., Yamanaka, M., Maeda, K., et al. 2009, [ApJ](#), **700**, 1680
- Tanikawa, A., Sato, Y., Nomoto, K., et al. 2017, [ApJ](#), **839**, 81
- Taubenberger, S., Valenti, S., Benetti, S., et al. 2009, [MNRAS](#), **397**, 677
- Tauris, T. M., Langer, N., Moriya, T. J., et al. 2013, [ApJL](#), **778**, L23
- Tauris, T. M., Langer, N., & Podsiadlowski, P. 2015, [MNRAS](#), **451**, 2123
- Tayal, S. S. 2004, [ApJS](#), **153**, 581
- Theureau, G., Hanski, M. O., Coudreau, N., Hallet, N., & Martin, J.-M. 2007, [A&A](#), **465**, 71
- Valenti, S., Benetti, S., Cappellaro, E., et al. 2008, [MNRAS](#), **383**, 1485
- Valenti, S., Yuan, F., Taubenberger, S., et al. 2014, [MNRAS](#), **437**, 1519
- Waldman, R., Sauer, D., Livne, E., et al. 2011, [ApJ](#), **738**, 21
- Wanajo, S., Janka, H.-T., & Müller, B. 2013, [ApJL](#), **767**, L26
- Weiler, K. W., Panagia, N., Montes, M. J., & Sramek, R. A. 2002, [ARA&A](#), **40**, 387
- Wellons, S., Soderberg, A. M., & Chevalier, R. A. 2012, [ApJ](#), **752**, 17
- Woosley, S. E., & Heger, A. 2007, [PhR](#), **442**, 269
- Woosley, S. E., & Heger, A. 2015, [ApJ](#), **810**, 34
- Woosley, S. E., & Kasen, D. 2011, [ApJ](#), **734**, 38
- Yaron, O., & Gal-Yam, A. 2012, [PASP](#), **124**, 668
- Yuan, F., Kobayashi, C., Schmidt, B. P., et al. 2013, [MNRAS](#), **432**, 1680
- Zapartas, E., de Mink, S. E., Izzard, R. G., et al. 2017, [A&A](#), **601**, A29